European Journal of Mechanics / A Solids 105 (2024) 105238

Contents lists available at ScienceDirect

European Journal of Mechanics / A Solids

journal homepage: www.elsevier.com/locate/ejmsol

Full length article

A homogenization-based model of the Gurson type for porous metals comprising randomly oriented spheroidal voids

S. Xenos [a,b], N. Aravas [b,c], K. Danas [a,d,*]

[a] LMS, C.N.R.S, École Polytechnique, Institut Polytechnique de Paris, Palaiseau, 91128, France
[b] Department of Mechanical Engineering, University of Thessaly, 38334, Volos, Greece
[c] International Institute for Carbon Neutral Energy Research (WPI-I2CNER), Kyushu University, 744 Moto-oka, Nishi-ku, Fukuoka 819-0395, Japan
[d] ELyTMaX, CNRS, Tohoku University, Sendai, Japan

ARTICLE INFO

Keywords:
Porous materials
Ductile failure
Finite elements
Homogenization
Elasto-plasticity
Metal forming simulation

ABSTRACT

In this work, we propose a new fully explicit isotropic, rate-independent, elasto-plastic model for porous materials comprising a random with uniform probability, isotropic distribution of randomly oriented spheroidal voids of the same shape. The proposed model is based on earlier homogenization estimates that use a linear comparison composite theory. The resulting expressions exhibit the simplicity of the well known Gurson model and, thus, its numerical implementation in a finite element code is straightforward. To assess the accuracy of the analytical model, we carry out detailed finite-strain, three-dimensional finite element (FE) simulations of representative volume elements (RVEs) with the corresponding microstructures. Proper minimal parameter calibration of the model leads to fairly accurate agreement of the analytical predictions with the corresponding FE average stresses and porosity evolution. We show, both analytically and numerically, that the initial aspect ratio of the voids has a significant effect on the homogenized yield surface of the porous material leading to extremely soft responses for flat oblate voids (e.g. aspect ratio less than 0.5) especially at large triaxialities. Finally, after numerical implementation of the model in a commercial finite element code (ABAQUS), we solve the industrially important problem of hole expansion and comment on the role of porous compressible plasticity versus classical incompressible plasticity.

1. Introduction

The problem of ductile fracture of metallic materials is closely related to the distribution and evolution of voids in the underlying microstructure. The presence of these voids can be attributed either to manufacturing induced defects, interface decohesion between the matrix and dispersed secondary particles or particle breakage during deformation. The mechanisms driving the process may vary significantly depending on the loading conditions and the local stress states developed (Noell et al., 2018), however the most prominent ones involve the growth, nucleation and coalescence of voids (Pardoen and Hutchinson, 2000; Benzerga and Leblond, 2010; Benzerga et al., 2016).

Perhaps, the most well-known constitutive model for the description of the macroscopic behavior of porous ductile materials is that of Gurson (Gurson, 1977), which was derived using a combination of limit analysis and homogenization by considering a spherical void embedded into a rigid-plastic von Mises matrix while assuming that the void may change its size but not its shape during plastic deformation. Despite the model's inability to yield accurate predictions for shear dominated stress states due to its restrictive assumptions, the simplicity of the model's formulation and the versatility regarding its computational implementation have made it very attractive and several extensions have been proposed over the years. Phenomenological modifications to account for void nucleation and criteria for void coalescence were proposed soon after (Chu and Needleman, 1980; Tvergaard and Needleman, 1984), while modifications to include dependence on the third invariant J_3 of the stress deviator in order to account for shear failure effects were later proposed by several authors (Nahshon and Hutchinson, 2008; Zhou et al., 2014; Dæhli et al., 2018; He et al., 2021; Rousselier, 2022; Khan et al., 2023). Concerning the latter, such dependencies on physical grounds stem from the fact that in real materials, voids are not spherical but they may rather have irregular shapes, and this void shape effect can play a detrimental role in the predictions of ductile fracture. For example, finite element calculations conducted by Tvergaard (2009), Nielsen and Tvergaard (2011), and Nielsen et al. (2012) indicate that void shape changes or void rotations can reduce the load-carrying capacity of the material in shear-dominated loadings

* Corresponding author at: LMS, C.N.R.S, École Polytechnique, Institut Polytechnique de Paris, Palaiseau, 91128, France.
E-mail addresses: sokratis.xenos@polytechnique.edu (S. Xenos), aravas@uth.gr (N. Aravas), konstantinos.danas@polytechnique.edu (K. Danas).

https://doi.org/10.1016/j.euromechsol.2024.105238
Received 20 August 2023; Received in revised form 13 December 2023; Accepted 9 January 2024
Available online 11 January 2024
0997-7538/

without increase in porosity due the interaction of flattened, crack-like neighboring voids (Anderson et al. (1990)).

In this regard, various models have been proposed in the literature that assume more general void shapes and/or void rotation. Among others, notable references are the models proposed by Leblond and co-workers (Gologanu et al., 1993, 1994, 1997) for spheroidal voids and Madou and Leblond (Madou and Leblond, 2012a,b) for general ellipsoidal voids. These models, which were also derived through a limit analysis approach on appropriately selected representative cells by using kinematically admissible velocity fields, serve as extensions to the Gurson model that incorporate void shape effects. However, even though these models take into account more general void shapes and their evolution, they do not assess void rotation in a seamless manner. Another more rigorous class of homogenization models for porous materials was proposed by Kailasam et al. (1997), Kailasam and Ponte Castañeda (1998) in the general context of viscoplasticity. These were developed based on the variational principles initially presented in the works of Ponte Castañeda (1991) and Willis (1991) on homogenization of nonlinear composites providing an upper bound for the effective yield function of the porous material using a linear comparison composite (LCC) methodology. Even though in these models void rotation due to plastic deformation is accounted for, bounds derived with this methodology were found to be very stiff in the case of materials with an isotropic matrix and spherical voids subjected to large hydrostatic loadings (Michel and Suquet, 1992). Modifications to existing models (e.g. Danas and Aravas (2012)) and improved (but more complex) models derived using similar principles (Danas et al., 2008b; Danas and Ponte Castañeda, 2009a,b; Agoras and Ponte Castañeda, 2013) were later proposed in an effort to amend these issues. Moreover, expressions from those homogenization models were directly borrowed in the limit analysis based models mentioned previously to include void orientation changes (Madou et al., 2013; Morin et al., 2017).

The aforementioned models share some common characteristics: (i) they assume a first order effect on void shape and/or void orientation evolution (put in other words: on anisotropy induced due to void shape changes) on the related mechanisms that lead to ductile fracture and (ii) they consider microstructures comprising uniform or via composite sphere/ellipsoidal assemblage type distributions of ellipsoidal voids that all have the *same orientation* (unidirectional microstructures). More often than not, the initial microstructure is assumed to comprise *spherical* voids to start off with an initially isotropic response. Nevertheless, metallic materials usually contain an initial distribution of non-spherical, irregularly shaped pores (Wang et al., 2021; Limodin et al., 2023). Those pores have rather flat shapes that can be even considered cracks and are randomly oriented in space (Meynard et al., 2022). Yet, the response of these materials remains fairly isotropic in the early stages of deformation implying that those shapes are distributed with a rather random orientation.

In this view, earlier numerical and theoretical homogenization studies in elasticity (Gatt et al., 2005; Anoukou et al., 2018; Zerhouni et al., 2021) as well as limit analysis approaches for rigid-perfectly plastic materials (Vincent and Monerie, 2008; Shen et al., 2011) suggest that, the macroscopic properties of porous materials can be quite different, at the same porosity levels, for microstructures that consist of randomly orientated voids with different initial shapes. Such observations imply that initial void shape alone could potentially have important effects on the effective behavior and porosity evolution of the porous material and consequently on its overall ductility. A more realistic modeling approach would need to consider voids which are not necessarily all aligned in the same direction but are randomly oriented in the matrix. One way to investigate this effect would be a potential extension of the model proposed in Kailasam et al. (1997), Danas and Ponte Castañeda (2009a) or Danas and Aravas (2012) for the inclusion of multiple (but finite) void families with the same shape but different orientations; in that case the general theory presented by Kailasam (Kailasam and Ponte Castañeda, 1998) in the context of nonlinear homogenization for multiple-phase composites with "particulate" microstructures could be used. Application of such an approach is computationally inefficient in practice, since it would lead to a considerable increase of the underlying microstructural variables (porosity, void shape, and orientation evolution) that would need to be kept track of. The aim of this work is to showcase a computationally feasible way of addressing such randomly oriented void distributions accepting a certain level of calibration in the final model.

1.1. Scope of the study

In the present study, we propose a new rate-independent, elastic–plastic model for porous metals with *initially random void shape orientations* distributed randomly and isotropically in space. The model can be used to describe the effective response of metallic materials with a von Mises matrix; possible extensions to include dependence on the third invariant J_3 of the deviatoric stress can be easily incorporated in a heuristic manner for example along the lines described in Benzerga and Leblond (2010). The model takes an explicit form similar to that of Gurson, but it incorporates spheroidal voids, albeit randomly oriented, seamlessly through homogenization. This is achieved by the equivalence between projection into the space of isotropic fourth-order tensors and integral orientation averaging (Gatt et al. (2005), Moakher and Norris (2006)), leading to an overall isotropic elastic–plastic behavior. To keep the model simple with a minimum set of microstructural variables, all families of voids are assumed to have the same shape described by a single aspect ratio, which does not evolve with deformation but rather remains constant and acts as a parameter for the model. The idea for assuming a distribution of spheroids instead of general ellipsoids is twofold.

Firstly, the spheroidal voids cover the interesting special case of flat random oblate voids (spheroids with aspect ratio $w \to 0$), which in the limit of vanishing porosity correspond to random cracks (Willis (1977), Monchiet (2006)), and can have a detrimental impact on the load-carrying capacity of the material. This special case can be analyzed by using our results along with a procedure similar to the one presented in the works of Willis (Willis, 1977, 1980, 1981) who considered the aforementioned limits in order to derive estimates for the effective properties in the context of various physical problems.

Secondly, in the calculation of the so-called "microstructural" tensors for general ellipsoids that appear in the constitutive equations (see for example Aravas and Ponte Castañeda (2004)), elliptic integrals of the first and second kind need to be evaluated numerically, whereas, in the case of spheroidal voids, explicit analytical expressions can be obtained. This allows for a straightforward implementation of the model in finite element codes by using a methodology similar to that of the original Gurson model. As a result, the model can be efficiently used both for the investigation of void shape effects on the macroscopic behavior of the porous material and for the simulation of ductile fracture related problems in structural components.

The paper is organized as follows. Section 2 describes the proposed microstructure as well as the assumptions adopted in order to derive a fully explicit model. In Section 3, the theoretical framework of the proposed model is established. A decoupled procedure is used, in which elasticity and plasticity are treated separately and then put together to yield the elastic–plastic constitutive model. Instantaneous yield curves predicted by the analytical model for different microstructural configurations are presented in Section 4, and the effects of the void shape are investigated. In Section 5, finite element results from numerical homogenization calculations and model calibration are presented. In Section 6, the calibrated model is used to examine the predicted microstructural evolution in simple loading cases. The model is also implemented in a User MATerial (UMAT) subroutine in ABAQUS/Standard and a 3-dimensional numerical simulation of the quasi-static hole expansion test is performed.

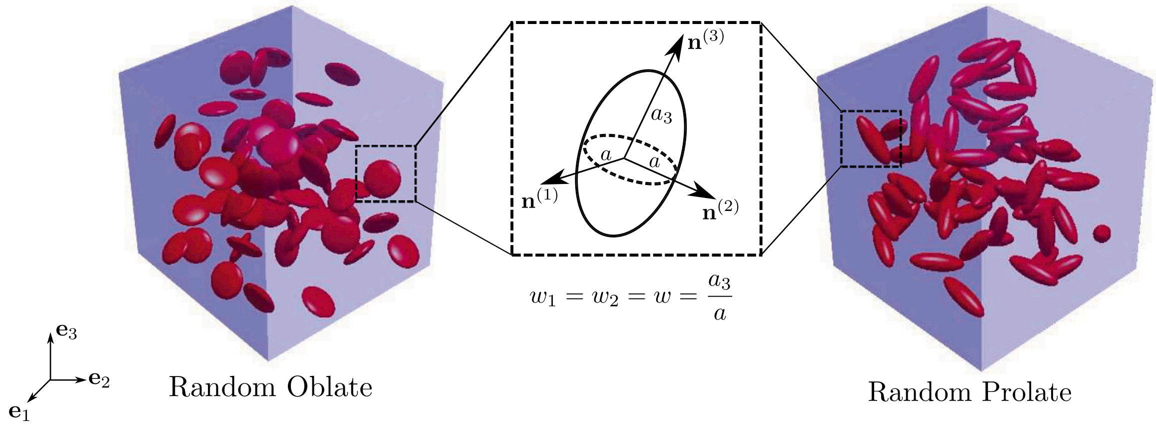

Fig. 1. Illustration of porous microstructures consisting of N_{fam} randomly oriented and randomly distributed spheroidal voids (shown in red). The aspect ratio is $w = 0.3$ in the oblate and $w = 5$ in the prolate voids.

Standard notation is used throughout. Boldface symbols denote tensors the orders of which are indicated by the context. All tensor components are written with respect to a fixed Cartesian coordinate system with base vectors $\mathbf{e}_i$ ($i = 1, 2, 3$), and the summation convention is used for repeated Latin indices, unless otherwise indicated. Let $\mathbf{a}$, $\mathbf{b}$ be vectors, $\mathbf{A}$, $\mathbf{B}$ second-order tensors, $\boldsymbol{\mathcal{C}}$, $\boldsymbol{\mathcal{D}}$ fourth-order tensors and $\mathbb{E}$, $\mathbb{F}$ eighth-order tensors. The following products are used in the text: $(\mathbf{a}\,\mathbf{b})_{ij} = a_i\, b_j$, $\mathbf{A} : \mathbf{B} = A_{ij}\, B_{ij}$, $(\mathbf{A} \cdot \mathbf{B})_{ij} = A_{ik}\, B_{kj}$, $(\mathbf{A}\,\mathbf{B})_{ijkl} = A_{ij}\, B_{kl}$, $(\boldsymbol{\mathcal{C}} : \mathbf{A})_{ij} = \mathcal{C}_{ijkl}\, A_{kl}$, $(\mathbf{A} : \boldsymbol{\mathcal{C}})_{ij} = A_{kl}\, \mathcal{C}_{klij}$, $(\boldsymbol{\mathcal{C}} : \boldsymbol{\mathcal{D}})_{ijkl} = \mathcal{C}_{ijpq}\, \mathcal{D}_{pqkl}$, $\boldsymbol{\mathcal{C}} :: \boldsymbol{\mathcal{D}} = \mathcal{C}_{ijkl}\, \mathcal{D}_{ijkl}$, $(\boldsymbol{\mathcal{C}}\,\boldsymbol{\mathcal{D}})_{ijklpqrs} = \mathcal{C}_{ijkl}\, \mathcal{D}_{pqrs}$ $(\mathbb{E} :: \boldsymbol{\mathcal{C}})_{ijkl} = \mathbb{E}_{ijklpqrs}\, \mathcal{C}_{pqrs}$, $(\boldsymbol{\mathcal{C}} :: \mathbb{E})_{ijkl} = \mathcal{C}_{pqrs}\, \mathbb{E}_{pqrsijkl}$, and $(\mathbb{E} :: \mathbb{F})_{ijklpqrs} = \mathbb{E}_{ijklmnyz}\, \mathbb{E}_{mnyzpqrs}$. The inverse $\boldsymbol{\mathcal{C}}^{-1}$ of a fourth-order tensor $\boldsymbol{\mathcal{C}}$ that has the "minor" symmetries $\mathcal{C}_{ijkl} = \mathcal{C}_{jikl} = \mathcal{C}_{ijlk}$ is defined so that $\boldsymbol{\mathcal{C}} : \boldsymbol{\mathcal{C}}^{-1} = \boldsymbol{\mathcal{C}}^{-1} : \boldsymbol{\mathcal{C}} = \boldsymbol{\mathcal{I}}$, where $\boldsymbol{\mathcal{I}}$ is the symmetric fourth-order identity tensor with Cartesian components $\mathcal{I}_{ijkl} = (\delta_{ik}\, \delta_{jl} + \delta_{il}\, \delta_{jk})/2$, δ_{ij} being the Kronecker delta.

2. Microstructure description

We consider porous metals with random microstructures that contain $N_{\mathtt{fam}}$ families of randomly distributed ellipsoidal voids of different shapes and orientations embedded in an isotropic elasto-plastic matrix (to be defined explicitly later). We follow the definitions introduced in Anoukou et al. (2018): each family contains voids with the same aspect ratios and orientation but possibly different sizes, e.g., polydisperse microstructures (Lopez-Pamies et al., 2013). The features of the vacuous phase can be described by the following set of microstructural variables (see Fig. 1):

- The void volume fraction or porosity $f = \mathcal{V}^v/\mathcal{V}$, where $\mathcal{V}^v$ denotes the volume occupied by the voids and $\mathcal{V}$ the total volume of the specimen. The volume fraction of the matrix is $1 - f$.
- Two aspect ratios that characterize the shape of the ellipsoidal voids for each void family: $w_1^{\mathtt{I}} = a_3/a_1$ and $w_2^{\mathtt{I}} = a_3/a_2$ with $\mathtt{I} = 1, \ldots, N_{\mathtt{fam}}$.
- A set of three mutually orthogonal unit vectors that define the orientation of the principal axes in the ellipsoidal voids of each void family: $\{\mathbf{n}_{\mathtt{I}}^{(1)}, \mathbf{n}_{\mathtt{I}}^{(2)}, \mathbf{n}_{\mathtt{I}}^{(3)}\}$ with $\mathtt{I} = 1, \ldots, N_{\mathtt{fam}}$.

It has been shown recently that such microstructures may be directly realized by the use of 3D-printers (Zerhouni et al., 2019; Tarantino et al., 2019; Hooshmand-Ahoor et al., 2022).

We consider the geometries described above as idealized microstructures for low-porosity metallic materials. Actual metallic materials do not have such regular quadric pore shapes (Limodin et al., 2023); nevertheless, over the last fifty years, such idealized geometries have been used extensively to adequately account for the main effects of porosity on ductile fracture (Gurson, 1977; Tvergaard and Needleman, 1984; Kailasam and Ponte Castañeda, 1998; Danas and Ponte Castañeda, 2009a; Madou and Leblond, 2012a; Danas and Aravas, 2012; Morin et al., 2016). These involve the first order porosity effect as well as the local *average* pore-induced morphological anisotropy due to random grain distributions and precipitates. An ellipsoidal void should be regarded as a locally orthotropic soft heterogeneity, which describes the average response over a neighborhood of voided regions. Any attempt to connect the actual local microstructure of a real material with such idealized void shape distributions is irrelevant. A local pore description requires a practically unattainable meshing effort and extremely heavy numerical simulations that would not even allow for large strains at the macroscopic scale. In turn, the idealized average ellipsoidal voids allow for the development of simple models that can be calibrated and used to address boundary value problems at the scale of structural components (Danas and Aravas, 2012; Morin et al., 2017).

A priori, the linear comparison composite (LCC) homogenization models proposed by Ponte Castañeda (1991) and co-workers may deal with such ideal microstructures and any number $N_{\mathtt{fam}}$ of families (see for instance (Papadioti et al., 2016)), owing mainly to the corresponding linear composite estimates they depend on Willis (1981).

Using the same viewpoint, we simplify further the microstructure descriptors in an attempt to propose a fully analytical and explicit, *isotropic* model. The simplifications introduced are as follows.

- All void families have the same shape, i.e., $w_1^{\mathtt{I}} = w_1$ and $w_2^{\mathtt{I}} = w_2$ (for all $\mathtt{I} = 1, \ldots, N_{\mathtt{fam}}$), but not the same orientation.
- All voids are assumed spheroidal, i.e., $w_1 = w_2 = w$, so that the semi-axes become $a_1 = a_2 = a$. The cases of $w = 1$, $w > 1$, and $w < 1$ correspond to spherical, prolate, and oblate spheroidal voids respectively. This additional specification allows for the development of a fully explicit model of the Gurson type, since the Eshelby–Hill tensors (Eshelby (1957), Hill (1963)) involved in the homogenization estimates can now be determined analytically as described in Appendix A and, in more detail, in Willis (1981). Note that the special cases $w_1 = a_3/a_1 = 1$ and $w_2 \neq 1$ (or $w_1 \neq 1$ and $w_2 = a_3/a_2 = 1$) also correspond to spheroidal voids rotated by 90° about $\mathbf{e}_1$ (or $\mathbf{e}_2$) and therefore included by default in the formulation.
- We consider a spatially uniform (isotropic) random distribution of orientations of the spheroidal voids leading to an overall isotropic elasto-plastic response of the porous material. In the analytical treatment of the model presented in Section 3, an infinite number of orientations is considered and an integral orientation average is calculated (see Appendix B). In the numerical microstructure generation of a representative volume element, a finite number $N_{\mathtt{fam}}$ of families with random orientations is used (see Anoukou et al. (2018)). The number of voids deemed sufficient for a fairly

isotropic average RVE response is decided by simulating RVEs with progressively more voids until the response does not change in the three principal directions beyond a small percentage. This important point is discussed in more detail in Section 5.1.2.

A representation of such random porous (or more generally particulate) microstructures with oblate (i.e., $w = 0.3$) and prolate (i.e., $w = 5$) voids is shown in Fig. 1.

Remark 1. It should be noted at this point that, for the sake of deriving a fully explicit and computationally efficient analytical homogenization model, only microstructures with statistically uniform distribution of voids will be considered. Clustering effects at microstructural level, such as the ones discussed in the work of Bilger et al. (2007) and more recently (Holte et al., 2023), will not be taken into account. However, the present model can account for such effects at a macroscopic level in an average sense since non-uniform initial porosity distributions can be readily implemented in codes used for structural calculations (see for instance (Srivastava et al., 2014)).

3. The isotropic projection model

In the following, we describe the main ingredients of the proposed analytical model. An additive decomposition of the total rate-of-deformation tensor $\mathbf{D}$ into an elastic and a plastic part is used:

$$\mathbf{D} = \mathbf{D}^e + \mathbf{D}^p \tag{3.1}$$

The constitutive equations for the elastic and plastic behavior are treated in a decoupled manner (e.g., Cheng et al. (2017)) and are later combined in order to yield the total effective elastic–plastic response of the porous material.

3.1. Elasticity

The *homogenized* elastic behavior of the porous material is described by a hypoelastic constitutive equation of the form

$$\mathbf{D}^e = \boldsymbol{\mathcal{M}} : \overset{\nabla}{\boldsymbol{\sigma}}, \qquad \boldsymbol{\mathcal{M}} = \frac{1}{2\,\mu}\boldsymbol{\mathcal{K}} + \frac{1}{3\,\kappa}\boldsymbol{\mathcal{J}}, \qquad \boldsymbol{\mathcal{J}} = \frac{1}{3}\boldsymbol{\delta}\,\boldsymbol{\delta}, \qquad \boldsymbol{\mathcal{K}} = \boldsymbol{\mathcal{I}} - \boldsymbol{\mathcal{J}}, \tag{3.2}$$

where, $\overset{\nabla}{\boldsymbol{\sigma}}$ is the co-rotational Jaumann derivative of the Cauchy stress $\boldsymbol{\sigma}$, $\boldsymbol{\mathcal{I}}$ is the symmetric fourth-order identity tensor defined in the Introduction, $(\boldsymbol{\mathcal{K}}, \boldsymbol{\mathcal{J}})$ are the deviatoric and hydrostatic fourth-order identity tensors and $\boldsymbol{\delta}$ is the second-order identity tensor (Kronecker delta). In turn, $\boldsymbol{\mathcal{M}}$ is the fourth-order *isotropic* incremental elastic compliance tensor, and (κ, μ) are the effective incremental elastic bulk and shear moduli of the porous material with an infinite number of randomly oriented pore families ($N_{\mathtt{fam}} \to \infty$), which all have the same aspect ratio w, as discussed in the previous section.

Specifically, the incremental elastic moduli (κ, μ) (and thus $\boldsymbol{\mathcal{M}}$) are calculated using the methodology of Gatt et al. (2005) (see also Anoukou et al. (2018)), who proposed the use of an "isotropic projection" of the well-known anisotropic (Hashin and Shtrikman, 1963) estimates, and take the final compact and explicit form

$$\frac{1}{3\,\kappa} = \frac{1}{3}\mathcal{M}^{\mathtt{w}}_{iijj} \qquad \text{and} \qquad \frac{1}{2\,\mu} = \frac{1}{5}\left(\mathcal{M}^{\mathtt{w}}_{ijij} - \frac{1}{3\,\kappa}\right). \tag{3.3}$$

In this expression, $\boldsymbol{\mathcal{M}}^{\mathtt{w}}$ is the effective compliance tensor corresponding to a single family of unidirectional ellipsoidal voids (Aravas and Ponte Castañeda, 2004; Danas, 2008)[1]

$$\boldsymbol{\mathcal{M}}^{\mathtt{w}}(\mu_{\mathtt{m}}, \kappa_{\mathtt{m}}, \nu_{\mathtt{m}}, f, w, \mathbf{n}^{(i)}) = \boldsymbol{\mathcal{M}}^{\mathtt{m}}(\mu_{\mathtt{m}}, \kappa_{\mathtt{m}}) + \frac{f}{(1-f)\mu_{\mathtt{m}}}\boldsymbol{\mathcal{Q}}^{-1}(\nu_{\mathtt{m}}, w, \mathbf{n}^{(i)}), \tag{3.4}$$

[1] A general expression for the effective compliance tensor of a composite containing N different type of inclusions is given by Willis (see Willis (1982), p. 671).

where

$$\boldsymbol{\mathcal{M}}^{\mathtt{m}} = \frac{1}{2\,\mu_{\mathtt{m}}}\boldsymbol{\mathcal{K}} + \frac{1}{3\,\kappa_{\mathtt{m}}}\boldsymbol{\mathcal{J}},$$

$(\mu_{\mathtt{m}}, \kappa_{\mathtt{m}})$ are the shear modulus and bulk modulus of the matrix and $\nu_{\mathtt{m}} = (3\,\kappa_{\mathtt{m}} - 2\,\mu_{\mathtt{m}})/(6\,\kappa_{\mathtt{m}} + 2\,\mu_{\mathtt{m}})$ the matrix Poisson's ratio. Also, $\boldsymbol{\mathcal{Q}}$ is a fourth-order "microstructural" tensor related directly to the well-known Eshelby–Hill tensor (Eshelby, 1957; Hill, 1963) and has both the major ($\mathcal{Q}_{ijkl} = \mathcal{Q}_{klij}$) and minor symmetries ($\mathcal{Q}_{ijkl} = \mathcal{Q}_{jikl} = \mathcal{Q}_{ijlk} = \mathcal{Q}_{jilk}$). Methodologies for the calculation of the components of $\boldsymbol{\mathcal{Q}}$ tensor for general *ellipsoids* can be found in various works (e.g., see Appendix A in Aravas and Ponte Castañeda (2004)[2]). In the case of *spheroidal* voids, which is the focus of the present work, these expressions simplify considerably becoming analytical and explicit and are presented in Appendix A.

In order to obtain the final expression (3.3), we define, next, the eighth-order "isotropic projection tensor" $\mathbb{P}\mathrm{roj}_{\{\boldsymbol{\mathcal{K}},\boldsymbol{\mathcal{J}}\}}$ (Gatt et al., 2005)

$$\mathbb{P}\mathrm{roj}_{\{\boldsymbol{\mathcal{K}},\boldsymbol{\mathcal{J}}\}} \equiv \frac{1}{\boldsymbol{\mathcal{K}} :: \boldsymbol{\mathcal{K}}}\boldsymbol{\mathcal{K}}\,\boldsymbol{\mathcal{K}} + \frac{1}{\boldsymbol{\mathcal{J}} :: \boldsymbol{\mathcal{J}}}\boldsymbol{\mathcal{J}}\,\boldsymbol{\mathcal{J}} = \frac{1}{5}\boldsymbol{\mathcal{K}}\,\boldsymbol{\mathcal{K}} + \boldsymbol{\mathcal{J}}\,\boldsymbol{\mathcal{J}}, \tag{3.5}$$

and identify $\boldsymbol{\mathcal{M}}$ with the isotropic projection $\mathbb{P}\mathrm{roj}_{\{\boldsymbol{\mathcal{K}},\boldsymbol{\mathcal{J}}\}} :: \boldsymbol{\mathcal{M}}^{\mathtt{w}}$ of $\boldsymbol{\mathcal{M}}^{\mathtt{w}}$, i.e.,

$$\boldsymbol{\mathcal{M}} = \mathbb{P}\mathrm{roj}_{\{\boldsymbol{\mathcal{K}},\boldsymbol{\mathcal{J}}\}} :: \boldsymbol{\mathcal{M}}^{\mathtt{w}} = \boldsymbol{\mathcal{M}}^{\mathtt{w}} :: \mathbb{P}\mathrm{roj}_{\{\boldsymbol{\mathcal{K}},\boldsymbol{\mathcal{J}}\}} \equiv \frac{1}{2\,\mu}\boldsymbol{\mathcal{K}} + \frac{1}{3\,\kappa}\boldsymbol{\mathcal{J}}, \tag{3.6}$$

leading to (κ, μ) defined in (3.3). This final result is obtained by direct algebraic manipulations and the use of the following identities

$$\boldsymbol{\mathcal{K}} :: \boldsymbol{\mathcal{K}} = 5, \qquad \boldsymbol{\mathcal{J}} :: \boldsymbol{\mathcal{J}} = 1, \qquad \boldsymbol{\mathcal{K}} :: \boldsymbol{\mathcal{J}} = \boldsymbol{\mathcal{J}} :: \boldsymbol{\mathcal{K}} = 0,$$
$$\boldsymbol{\mathcal{I}} :: \boldsymbol{\mathcal{I}} = 6, \qquad \boldsymbol{\mathcal{I}} :: \boldsymbol{\mathcal{K}} = \boldsymbol{\mathcal{K}} :: \boldsymbol{\mathcal{I}} = 5, \qquad \boldsymbol{\mathcal{I}} :: \boldsymbol{\mathcal{J}} = \boldsymbol{\mathcal{J}} :: \boldsymbol{\mathcal{I}} = 1.$$

which imply also that

$$\mathbb{P}\mathrm{roj}_{\{\boldsymbol{\mathcal{K}},\boldsymbol{\mathcal{J}}\}} :: \mathbb{P}\mathrm{roj}_{\{\boldsymbol{\mathcal{K}},\boldsymbol{\mathcal{J}}\}} = \mathbb{P}\mathrm{roj}_{\{\boldsymbol{\mathcal{K}},\boldsymbol{\mathcal{J}}\}}, \tag{3.7}$$

$$\mathbb{P}\mathrm{roj}_{\{\boldsymbol{\mathcal{K}},\boldsymbol{\mathcal{J}}\}} :: \left(\mathbb{P}\mathrm{roj}_{\{\boldsymbol{\mathcal{K}},\boldsymbol{\mathcal{J}}\}} :: \boldsymbol{C}\right) = \mathbb{P}\mathrm{roj}_{\{\boldsymbol{\mathcal{K}},\boldsymbol{\mathcal{J}}\}} :: \boldsymbol{C}, \tag{3.8}$$

for all fourth-order tensors $\boldsymbol{C}$ that possess major and minor symmetries. In addition, the last two relations are satisfied by all "projection operators" (e.g., see Meyer (2000), p. 386) and state the fact that the projection of a projection equals the original projection.[3]

Remark 2. In Appendix B, we show that the isotropic projection of a fourth-order tensor $\boldsymbol{C}$ that possesses the "minor" symmetries $C_{ijkl} = C_{jikl} = C_{ijlk} = C_{jilk}$ is equivalent to orientational averaging over all directions of $\boldsymbol{C}$. Therefore, the resulting effective elastic shear and bulk moduli (κ, μ) of the isotropic porous material resulting from the isotropic projection (3.6) of $\boldsymbol{\mathcal{M}}^{\mathtt{w}}$ are independent of the orientation vectors $\mathbf{n}^{(i)}$ and depend only on the elastic properties of the matrix ($\mu_{\mathtt{m}}$, $\kappa_{\mathtt{m}}$), on porosity f, and on the void aspect ratio w, as expected.

Fig. 2 shows the variation of the effective elastic moduli (μ, κ), determined from (3.3), with the aspect ratio w of the spheroidal voids and the bulk modulus $\kappa_{\mathtt{m}}$ of the matrix. All moduli in Fig. 2 are normalized with the shear modulus $\mu_{\mathtt{m}}$ of the matrix material; the horizontal axes are in a logarithmic scale.

Fig. 2a shows the effect of the aspect ratio w on the normalized effective shear $\mu/\mu_{\mathtt{m}}$ and bulk $\kappa/\mu_{\mathtt{m}}$ moduli of the porous material for a matrix with a ratio of bulk to shear modulus $\kappa_{\mathtt{m}}/\mu_{\mathtt{m}} = 2.17$ (corresponding to a Poisson's ratio of $\nu_{\mathtt{m}} = 0.3$). There is a significant drop in both the effective shear and bulk moduli for values of $w < 0.1$ (i.e., for penny shaped voids), whereas the stiffest response corresponds to spherical voids ($w = 1$). In the limit $w \to 0$ for fixed porosity, both the effective shear and bulk moduli (μ, κ) become asymptotically zero. This may be

[2] Aravas and Ponte Castañeda (2004) use the notation $\mathbf{Q} = \mu_m \boldsymbol{\mathcal{Q}}$ or $\mu_m \mathbf{Q}^{-1} = \boldsymbol{\mathcal{Q}}^{-1}$.

[3] All projection operators are "idempotent", i.e., they can be applied multiple times without changing the result beyond the initial application.

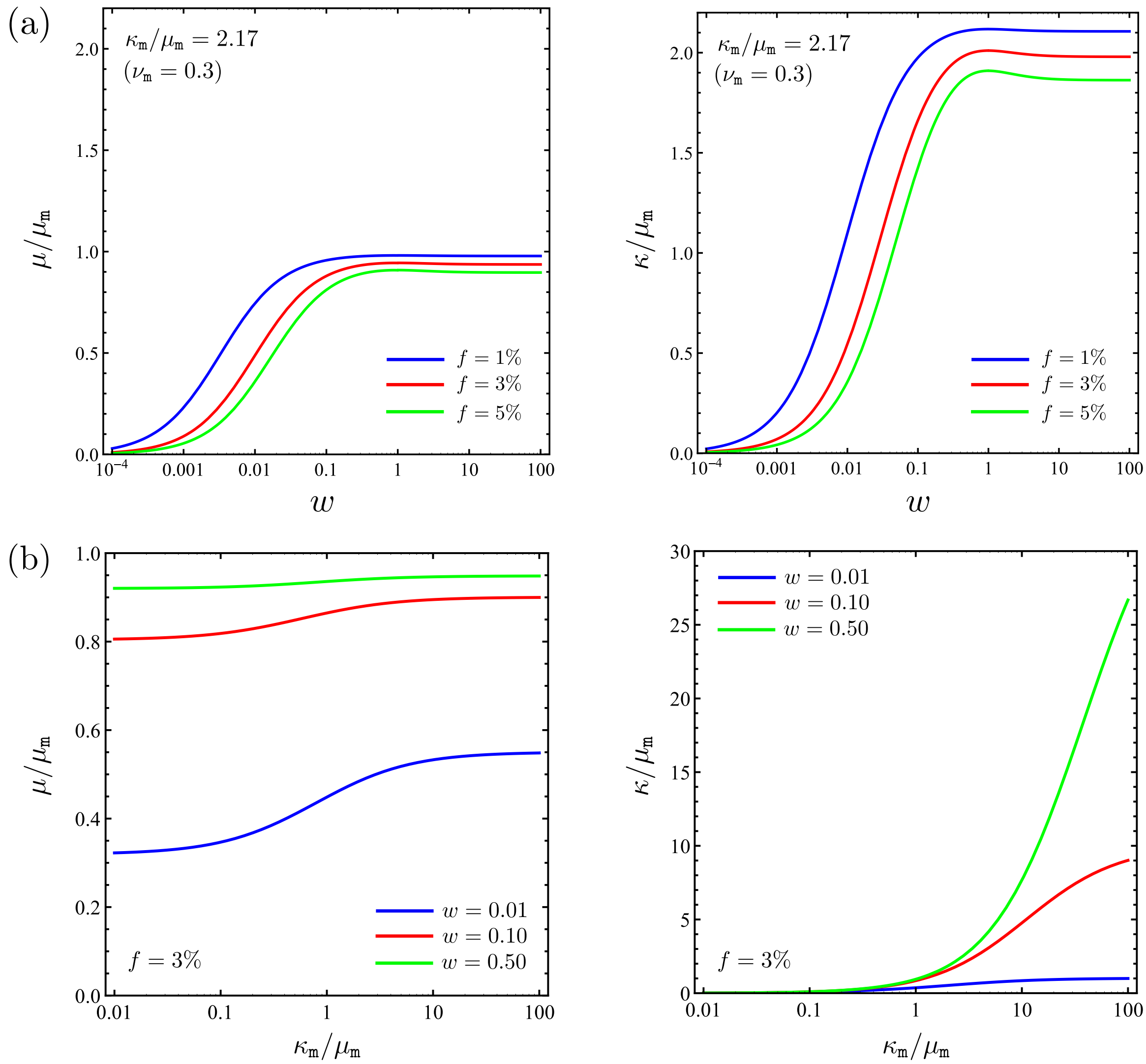

Fig. 2. Variation of the effective elastic shear and bulk moduli (μ, κ) with (a) the aspect ratio w of the spheroidal voids for $\nu_m = 0.3$ and for porosities 1%, 3% and 5%, and (b) the bulk modulus κ_m of the matrix material for a porosity of 3% and for aspect ratios $w = 0.01$, 0.10, and 0.50. All moduli are normalized with the shear modulus μ_m of the matrix material, and a logarithmic scale is used on the horizontal axes. Note the different scales used on the vertical axes in Fig. 2b.

interpreted by observing that, in the limiting case of $w \to 0$ with finite porosity, the porous material reaches a laminated type microstructure (with random orientations) and a plane of voided material may span the entire volume leading to zero resistance to deformation. These results are in agreement with the earlier numerical and theoretical homogenization studies of Gatt et al. (2005) and Anoukou et al. (2018).

The effect of the matrix bulk modulus κ_m on the effective elastic properties is shown in Fig. 2b for three different oblate void shapes at a fixed porosity value $f = 3\%$. Both the effective shear and bulk moduli (μ, κ) increase with increasing κ_m. However, the effective bulk modulus κ is much more sensitive to κ_m compared to the effective bulk modulus μ (note the different scales used on the vertical axes in Fig. 2b). For a fixed value of porosity ($f = 3\%$ in Fig. 2b), when κ_m takes large values, i.e., as the matrix approaches the incompressible limit, the effective bulk modulus κ defined in (3.3) reaches a finite value, which is an increasing function of w. In other words, as the aspect ratio w of the voids increases, the compressibility of the composite decreases.

The limiting case in which both $w \to 0$ and $f \to 0$ corresponds to a compressible cracked material and can be treated by using similar methods as the ones presented in the works of Willis (Willis, 1977, 1980, 1981); the details of such calculation will be addressed in a future publication.

Qualitatively similar results to those of Fig. 2b were found to hold for prolate voids (i.e., for $w > 1$), the only difference being that the effects of κ_m on the effective elastic moduli (μ, κ) remained the same with increasing w and are not presented here for brevity.

Finally, it is noted that this work deals with monotonic loads and thus porosity evolution during elastic loads is ignored since it is negligible. Nevertheless, possible extension of this model in the case of cyclic loads requires to consider porosity evolution in the elasticity regime. This may be added in the present model in a straightforward manner following the work of Cheng et al. (2017).

3.2. Plasticity and evolution of microstructure

In this section, we extend the previous ideas of void orientational averaging in the context of plasticity. In previous works, a form of orientational averaging was used by Vincent and Monerie (2008) and Shen et al. (2011) to derive the yield criterion. These models are based on a limit analysis approach and were found to be fairly accurate when compared to numerical yield surface estimates, but have not been as yet used to predict porosity evolution to the knowledge of the authors.

The present study is based on the linear comparison composite (LCC) method (Ponte Castañeda, 1991) and orientational averaging is used on the homogenized effective compliance tensor of the LCC. Calculation of porosity evolution is then a straightforward operation.

3.2.1. Yield function

For the determination of the yield function, the concept of isotropic projection, which was used in the description of the elastic constitutive equations, is now employed in a similar manner by making use of existing estimates for the rate-independent plastic behavior of porous materials from the literature (see for instance Danas and Aravas (2012)). More specifically, in this work, we propose a Gurson-type yield function, which however is obtained by use of the LCC homogenization method and in particular of the estimates for porous materials originally proposed in Kailasam et al. (1997). The Hashin–Shtrikman character of these estimates imply that interaction between the randomly oriented voids is accounted for in the sense of one- and two-point correlation functions. In this regard, it was shown in earlier studies that such estimates are sufficiently accurate for porosities up to $15-20\%$ (see for instance (Lopez-Pamies et al., 2013; Papadioti et al., 2016; Anoukou et al., 2018; Luo et al., 2023)), which is more than sufficient for the purposes of the present study.

More precisely, by projecting in the isotropic space the fourth-order tensor m (see for notation Danas and Aravas (2012) and Cao et al. (2015)) and using the interpolation scheme for the hydrostatic parts proposed in Mbiakop et al. (2015b) (in equation (64) of that reference), we readily obtain the explicit, isotropic yield function (see detailed derivation in Appendix C)

$$\begin{aligned}\Phi(\sigma_e, p, \bar{\varepsilon}^p, f, w) = {} & \frac{1}{3\, m_{\mathcal{K}}(f,w)} \left(\frac{\sigma_e}{\sigma_y}\right)^2 + \\ & + \frac{4}{9\, m_{\mathcal{J}}(f,w)} \left[(1-\alpha(f,w))\, q_{\mathcal{J}}^2(f) \left(\frac{3\,p}{2\,\sigma_y}\right)^2 \right. \\ & \left. +\ 2\,\alpha(f,w) \left(\cosh\frac{3\,p}{2\,\sigma_y} - 1\right)\right] - \\ & - (1-f). \end{aligned} \tag{3.9}$$

In this expression, p is the hydrostatic stress (positive in tension), $\boldsymbol{\sigma}^d = \boldsymbol{\sigma} - p\,\boldsymbol{\delta}$ is the stress deviator, $\sigma_e = \sqrt{3\,\boldsymbol{\sigma}^d : \boldsymbol{\sigma}^d/2}$ is the von Mises equivalent stress and σ_y is the yield stress of the matrix, which can in general be a function of the accumulated plastic strain $\bar{\varepsilon}^p$ of the matrix phase (i.e., $\sigma_y = \sigma_y(\bar{\varepsilon}^p)$). Moreover, we have that

$$\frac{1}{3\, m_{\mathcal{J}}(f,w)} = \frac{1}{3} m^{\mathrm{w}}_{iijj}, \quad \frac{1}{2\, m_{\mathcal{K}}(f,w)} = \frac{1}{5}\left(m^{\mathrm{w}}_{ijij} - \frac{1}{3\, m_{\mathcal{J}}}\right),$$
$$q_{\mathcal{J}}(f) = \frac{1-f}{\sqrt{f}\,\ln\frac{1}{f}}. \tag{3.10}$$

Here, the effective homogenized coefficients $(m_{\mathcal{K}}, m_{\mathcal{J}})$ result from the isotropic projection of the microstructural fourth-order tensor (similar to the elastic case discussed in the previous section)

$$m^{\mathrm{w}}(f,w) = \frac{3}{2}\boldsymbol{\mathcal{K}} + \frac{3f}{1-f}\boldsymbol{Q}^{-1}(1/2, w), \tag{3.11}$$

with $\boldsymbol{Q}$ evaluated in the limit of $\nu_{\mathrm{m}} = 1/2$ and given in explicit form in Appendix A. In turn, the correction factor $q_{\mathcal{J}}$ in (3.10) is determined so that the exact results of the "Composite Sphere and Cylinder Assemblages" (CSA & CCA) of Hashin and of the Gurson (1977) model can be recovered for the special case of spherical and cylindrical void shapes respectively, when the loading is purely hydrostatic (see Danas and Aravas (2012) and Mbiakop et al. (2015b)).

Finally, the interpolation function $\alpha(f,w)$ in (3.9) is introduced to allow for a better calibration of the proposed model with corresponding finite element (FE) representative volume element (RVE) simulations conducted in Section 5. In particular, α should be chosen so that:

- $\alpha = 1$ when f is lower than a prescribed minimum porosity f_{min}, thus leading to a "cosh" type response in the hydrostatic limit, similar to that of the Gurson model. Cao et al. (2015) have shown that, when the voids are initially spherical, the "cosh" functional form is more accurate for porosities less than 1%.
- $\alpha = 0$ as $f \to 1$. The rate at which α goes to zero for larger porosities depends on the aspect ratio w and in general is slower as $w \to 0$, i.e., for small values of w, the weight of the "cosh" term is larger than that of the quadratic term in (3.9).

In view of the above, we propose the following exponential expression for α, i.e.,

$$\alpha(f,w) = \begin{cases} 1, & f < f_{\min}, \\ e^{-\frac{f_{\min}}{k(w)}(f - f_{min})}, & f \geq f_{\min}, \end{cases} \quad \text{and} \quad k(w) = A\,w + B, \tag{3.12}$$

with $A = -8.6\times10^{-4}, B = 1.06\times10^{-3}$ and $f_{\min} = 0.005$. For these values, the predictions of the proposed model are found to best fit the corresponding numerical FE calculations for the stress and porosity evolution presented in Section 5.2 and will be used in all subsequent calculations. In general, $\alpha(f,w)$ can be used as a calibration function to fit numerical or experimental data.

In the case of spherical voids ($w = 1$), when $\alpha = 0$, the proposed model reduces to the MVAR (Modified VARariational) model of Danas and Aravas (2012), whereas, for $\alpha = 1$, the GVAR (Gurson VARiational) model of Cao et al. (2015) is recovered. These two models take into account the evolution of porosity as well as the evolution of the aspect ratios and the orientations of the voids. Therefore, even when they are initially isotropic, they eventually develop a deformation-induced *anisotropy*, in general. To keep the proposed new model sufficiently accurate and, at the same time, as simple a possible, we consider only the evolution of the porosity and assume that change of the void aspect ratio w has a negligible effect, so that the model is always ***isotropic***; i.e., we adopt a formulation similar to the Gurson model, which is now enriched with an additional microstructural parameter, the fixed aspect ratio w of the voids.

Remark 3. The yield condition (3.9) can be written alternatively in terms of an "effective stress" σ^*, such that

$$\Phi(\boldsymbol{\sigma}, \bar{\varepsilon}^p, f, w) = \sigma^*(\sigma_e, p, f, w) - \sigma_y(\bar{\varepsilon}^p) = 0,$$

where σ^* is now defined *implicitly* from the condition

$$\frac{1}{3\, m_{\mathcal{K}}}\left(\frac{\sigma_e}{\sigma^*}\right)^2 + \frac{4}{9\, m_{\mathcal{J}}}\left[(1-\alpha)\, q_{\mathcal{J}}^2 \left(\frac{3\,p}{2\,\sigma^*}\right)^2 + 2\,\alpha\left(\cosh\frac{3\,p}{2\,\sigma^*} - 1\right)\right] - (1-f) = 0.$$

This form of the yield condition is convenient, when a viscoplastic (rate-dependent) version of the model is of interest. In such a case, the flow stress σ_y depends on both $\bar{\varepsilon}^p$ and the plastic strain-rate $\dot{\bar{\varepsilon}}^p$ and an "overstress" can be defined in terms of the effective stress σ^*. An alternative and perhaps more rigorous way to include rate-dependency is the use of the corresponding viscoplastic LCC estimates (Danas, 2008; Danas et al., 2008b). This, however, is beyond the scope of the present study.

Remark 4. We remark here that an alternative realistic modeling approach would be to extend the models of Kailasam et al. (1997), Danas and Ponte Castañeda (2009a) or Danas and Aravas (2012) and consider a finite number of void families with the same shape but different orientations. In such a case, the general homogenization theory of Kailasam and Ponte Castañeda (1998) for multiple-phase composites could be used. This, however, would lead to a large number of microstructural variables, along with corresponding evolution equations, and would render the model unnecessarily complicated and difficult to implement numerically or calibrate in real-life applications. As will be discussed in Section 5, the proposed isotropic model, with the appropriate choice of the fitting parameters A, B, and f_{min} in the interpolation function $\alpha(f,w)$, is able to reproduce very well the results of detailed unit cell FE simulations.

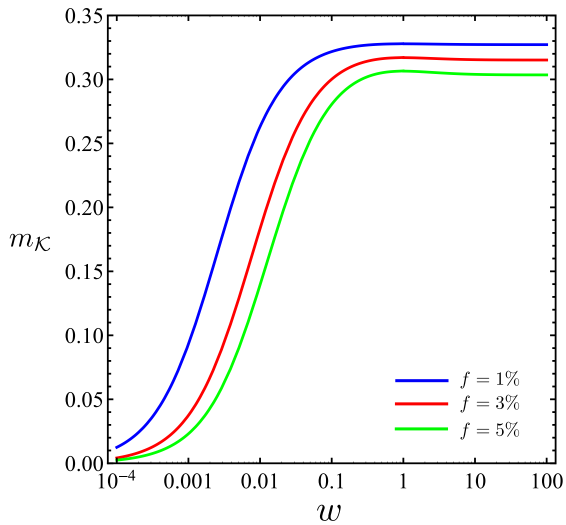

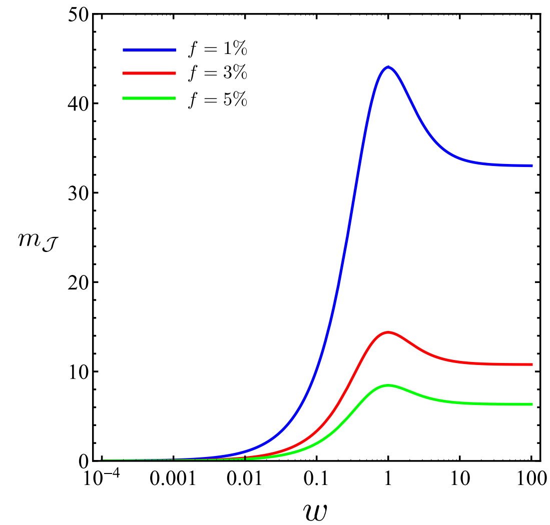

Fig. 3. Variation of the normalized effective plastic coefficients with void aspect ratio w (logarithmic scale) at three different porosity levels ($f = 1\%, 3\%, 5\%$). Note the different scales used on the vertical axes.

Fig. 3 shows the variation of the effective plastic coefficients $m_{\mathcal{K}}$ and $m_{\mathcal{J}}$ with the void aspect ratio w for three values of porosity ($f = 1\%, 3\%, 5\%$). Note the different scales used on the vertical axes. In Section 3.2.2 that follows, it is shown that the deviatoric and volumetric parts of the plastic deformation rate $\mathbf{D}^p$ are inversely proportional to $m_{\mathcal{K}}$ and $m_{\mathcal{J}}$, respectively (Eqs. (3.13)–(3.14) below). The results shown in Fig. 3 indicate that a porous material whose microstructure consists of isotropically distributed and randomly orientated oblate voids with low aspect ratios ($w < 0.1$) would exhibit a much *softer plastic response* compared to porous materials with spherical or prolate voids. It is also interesting to note that the effective plastic coefficient $m_{\mathcal{J}}$ associated with the hydrostatic response appears to be more sensitive to the shape of the voids compared to the effective plastic shear coefficient $m_{\mathcal{K}}$, especially at lower porosity levels. This implies that, for low values of porosity, the void shape affects strongly the plastic dilatational behavior of the material and, consequently, the corresponding porosity evolution during plastic deformation.

3.2.2. Flow rule and evolution equations

The plastic part of the rate-of-deformation tensor is given by the *associated flow rule* ("normality"), i.e.,

$$\mathbf{D}^p = \dot{\lambda}\,\mathbf{N}, \qquad \mathbf{N} \equiv \frac{\partial \Phi}{\partial \boldsymbol{\sigma}} = \frac{3}{2\,\sigma_e}\frac{\partial \Phi}{\partial \sigma_e}\boldsymbol{\sigma}^d + \frac{1}{3}\frac{\partial \Phi}{\partial p}\boldsymbol{\delta}, \tag{3.13}$$

where $\dot{\lambda} \geq 0$ is the "plastic multiplier", which vanishes when the response is elastic and is determined from the "consistency condition" $\dot{\Phi} = 0$ during plastic flow. The derivatives $\partial\Phi/\partial\sigma_e$ and $\partial\Phi/\partial p$ are calculated from (3.9):

$$\frac{\partial \Phi}{\partial \sigma_e} = \frac{2}{3\,m_{\mathcal{K}}}\frac{\sigma_e}{\sigma_y^2},$$
$$\frac{\partial \Phi}{\partial p} = \frac{4}{3\,m_{\mathcal{J}}}\frac{1}{\sigma_y}\left[(1-\alpha)q_{\mathcal{J}}^2\frac{3\,p}{2\,\sigma_y} + \alpha\sinh\left(\frac{3\,p}{2\,\sigma_y}\right)\right]. \tag{3.14}$$

In the present model, two variables evolve during plastic flow: (i) the accumulated plastic strain $\bar{\varepsilon}^p$ upon which depends the yield stress of the matrix σ_y and (ii) the porosity f. The first is an internal variable serving to characterize the plastic state in the matrix phase, and the second is a microstructural variable that characterizes the void volume fraction in the porous material.

For the evolution of $\bar{\varepsilon}^p$, we consider that the macroscopic plastic power $\boldsymbol{\sigma} : \mathbf{D}^p$ in the porous material is dissipated entirely in the plastic deformation of the matrix and equals the microscopic plastic power $(1-f)\sigma_y\,\dot{\bar{\varepsilon}}^p$, which leads to Tvergaard and Needleman (1984)

$$\dot{\bar{\varepsilon}}^p = \frac{\boldsymbol{\sigma} : \mathbf{D}^p}{(1-f)\sigma_y(\bar{\varepsilon}^p)} = \dot{\lambda}\frac{\boldsymbol{\sigma} : \mathbf{N}}{(1-f)\sigma_y(\bar{\varepsilon}^p)} \equiv \dot{\lambda}\,g_{\bar{\varepsilon}^p}. \tag{3.15}$$

The porosity evolution in the plastic regime is derived from mass conservation by ignoring the contribution of elasticity and taking into account the plastic incompressibility of the matrix material, such that

$$\dot{f} = (1-f)D_{kk}^p = \dot{\lambda}(1-f)N_{kk} \equiv \dot{\lambda}\,g_f. \tag{3.16}$$

3.3. The elastic–plastic tangent modulus

In the present section, we determine the elasto-plastic modulus $\boldsymbol{\mathcal{L}}^{ep}$, which is a fourth-order tensor that relates the Jaumann (or co-rotational) rate of the Cauchy stress $\overset{\nabla}{\boldsymbol{\sigma}}$ to the total rate-of-deformation tensor $\mathbf{D}$.

During plastic flow, $\mathbf{D}^e = \mathbf{D} - \mathbf{D}^p = \mathbf{D} - \dot{\lambda}\,\boldsymbol{\mathcal{L}} : \mathbf{N}$ and the elastic constitutive Eq. $(3.2)_1$ becomes

$$\overset{\nabla}{\boldsymbol{\sigma}} = \boldsymbol{\mathcal{L}} : \mathbf{D}^e = \boldsymbol{\mathcal{L}} : \mathbf{D} - \dot{\lambda}\,\boldsymbol{\mathcal{L}} : \mathbf{N}, \tag{3.17}$$

where $\boldsymbol{\mathcal{L}} = \boldsymbol{\mathcal{M}}^{-1} = 2\,\mu\,\boldsymbol{\mathcal{K}} + 3\,\kappa\,\boldsymbol{\mathcal{J}}$, with μ and κ defined in (3.3). The consistency condition $\dot{\Phi} = 0$ is written as

$$\begin{aligned}\dot{\Phi} &= \frac{\partial \Phi}{\partial \boldsymbol{\sigma}} : \overset{\nabla}{\boldsymbol{\sigma}} + \frac{\partial \Phi}{\partial \bar{\varepsilon}^p}\dot{\bar{\varepsilon}}^p + \frac{\partial \Phi}{\partial f}\dot{f} \\ &= \mathbf{N} : (\boldsymbol{\mathcal{L}} : \mathbf{D} - \dot{\lambda}\,\boldsymbol{\mathcal{L}} : \mathbf{N}) + \dot{\lambda}\frac{\partial \Phi}{\partial \bar{\varepsilon}^p}g_{\bar{\varepsilon}^p} + \dot{\lambda}\frac{\partial \Phi}{\partial f}g_f = 0\end{aligned}$$

where (3.17), (3.15), and (3.16) have been taken into account. The last equation yields

$$\dot{\lambda} = \frac{1}{L}\mathbf{N} : \boldsymbol{\mathcal{L}} : \mathbf{D}, \quad \text{where} \quad L = \mathbf{N} : \boldsymbol{\mathcal{L}} : \mathbf{N} + H \quad \text{with}$$
$$H = -\left(\frac{\partial \Phi}{\partial \bar{\varepsilon}^p}g_{\bar{\varepsilon}^p} + \frac{\partial \Phi}{\partial f}g_f\right). \tag{3.18}$$

The sign of the "hardening modulus" H determines whether the porous material is hardening ($H > 0$) or softening ($H < 0$) at the given stress state and internal and microstructural variables. Substitution of (3.18) in (3.17) yields the elasto-plastic tangent modulus $\boldsymbol{\mathcal{L}}^{ep}$, which reads

$$\overset{\nabla}{\boldsymbol{\sigma}} = \boldsymbol{\mathcal{L}}^{ep} : \mathbf{D}, \qquad \boldsymbol{\mathcal{L}}^{ep} = \boldsymbol{\mathcal{L}} - \frac{1}{L}(\boldsymbol{\mathcal{L}} : \mathbf{N})(\boldsymbol{\mathcal{L}} : \mathbf{N}). \tag{3.19}$$

Note that $\boldsymbol{\mathcal{L}}^{ep}$ has both the minor ($\mathcal{L}_{ijkl}^{ep} = \mathcal{L}_{jikl}^{ep} = \mathcal{L}_{ijlk}^{ep}$) and major ($\mathcal{L}_{ijkl}^{ep} = \mathcal{L}_{klij}^{ep}$) symmetries.

Remark 5. The numerical implementation of models, such as the one proposed, in finite element codes has been extensively discussed in the literature (e.g., see Section 3 in Aravas and Ponte Castañeda (2004) and Section 3.1 in Cao et al. (2015)). In this work, the proposed model is implemented in the general-purpose finite element code ABAQUS

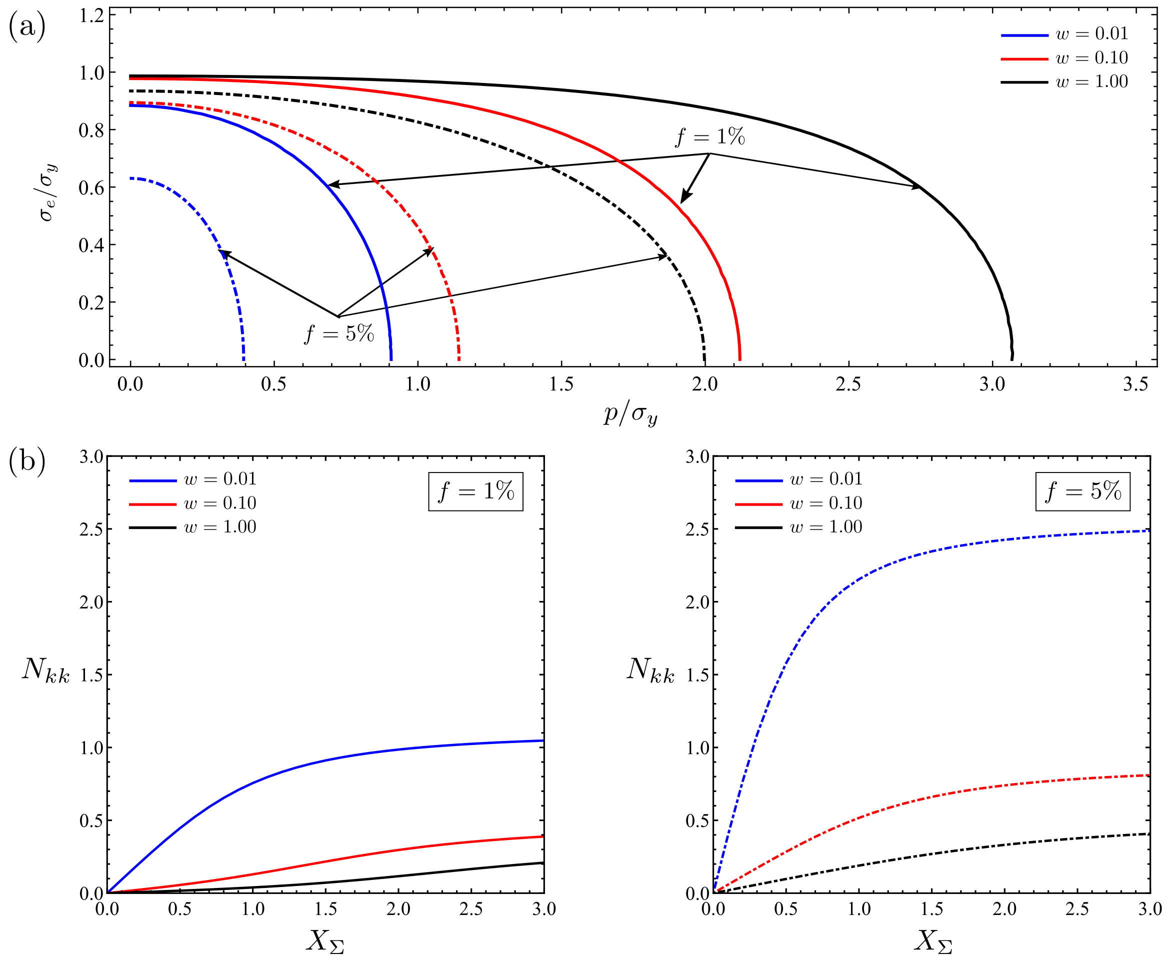

Fig. 4. (a) Yield curves on the normalized $p - \sigma_e$ plane. (b) Influence of void aspect ratio w on the variation of normalized volumetric plastic strain-rate N_{kk}; results are shown for porosities $f = 1\%$ (solid lines) and $f = 5\%$ (dashed lines).

via a User-MATerial (UMAT) subroutine. The numerical integration of the constitutive equations is similar to that used for the Gurson model and is based on the methodology of Aravas (1987). Alternatively, the implicit numerical integration algorithm proposed recently by Bouby et al. (2023) in the context of Generalized Standard Materials (GSM) could be used. This would require though the introduction of the "Lagrangian porosity" as an additional microstructural variable.

4. Results: Yield surfaces

To illustrate the effect of the void shape on the plastic behavior of the porous material, instantaneous yield curves on the normalized "meridonial" $p - \sigma_e$ plane are shown in Figs. 4–7. Since the isotropic yield function is independent of the Lode parameter (Danas et al., 2008b), only the results for the first quadrant are presented on the p–σ_e plane.

For later reference, we define the stress triaxiality and Lode angle[4] as

$$X_\Sigma = \frac{p}{\sigma_e}, \qquad \theta = \frac{1}{3}\arcsin\left(-\frac{27}{2}\frac{\det \boldsymbol{\sigma}^d}{\sigma_e^3}\right), \tag{4.1}$$

and the strain triaxiality as

$$X_E = \frac{E_m}{E_{eq}}, \qquad E_m = \frac{E_{kk}}{3}, \qquad E_{eq} = \sqrt{\frac{2}{3}\,\mathbf{E}^d : \mathbf{E}^d} \tag{4.2}$$

where E_m, E_{eq} are norms associated with the hydrostatic and deviatoric ($\mathbf{E}^d$) parts of the logarithmic strain tensor $\mathbf{E}$.

Fig. 4a shows the effect of the void shape on the effective yield curves for two different porosity values, $f = 1\%$ and 5%, and three different aspect ratios, $w = 0.01$, 0.10, and 1. Therein, we observe that as the aspect ratio w decreases from 1 to 0.01 (i.e., voids change from spherical to flat penny shape), the yield surfaces shrink significantly, especially at stress states near the "hydrostatic" point (the point on the curve corresponding to $\sigma_e = 0$ on the pressure axis). It should be also noted that, as the aspect ratio w decreases from 1 to 0.01, the hydrostatic point decreases faster than the corresponding "shear" point (the point on the curve corresponding to $p = 0$ on the σ_e-axis). Also, for a fixed value of the aspect ratio w, the yield surface shrinks with increasing porosity, as expected.

Fig. 4b shows the effects of stress triaxiality on the normalized volumetric plastic strain-rate $N_{kk} = D^p_{kk}/\dot{\lambda} = \partial\Phi/\partial p$, which is proportional to $\dot{f}$ and controls the evolution of porosity during plastic flow (see (3.13) and (3.16)). As the aspect ratio w decreases, the corresponding value for N_{kk} increases significantly for higher stress triaxialities, with the effect being more pronounced at higher porosities. This implies that, during plastic deformation and especially at high stress triaxiality conditions, porosity is expected to increase rapidly for microstructures consisting of flat oblate voids. Such effects are less important for prolate voids ($w > 1$) and are not shown here for brevity.

[4] It should be noted here that alternative definitions for θ can be found in the literature (see for instance Danas et al. (2008b) and Danas and Ponte Castañeda (2009a)) and any of them can be adopted, as long as consistency is kept in subsequent calculations.

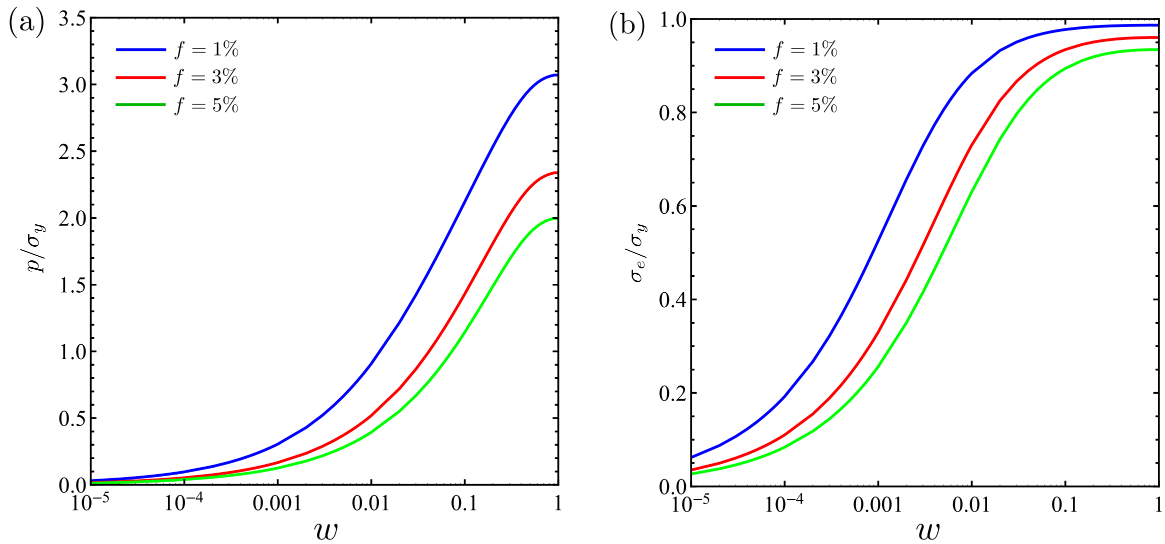

Fig. 5. Normalized (a) "hydrostatic" and (b) "shear" points as functions of the aspect ratio w (logarithmic scale) at three different porosity levels (f = 1%, 3%, and 5%).

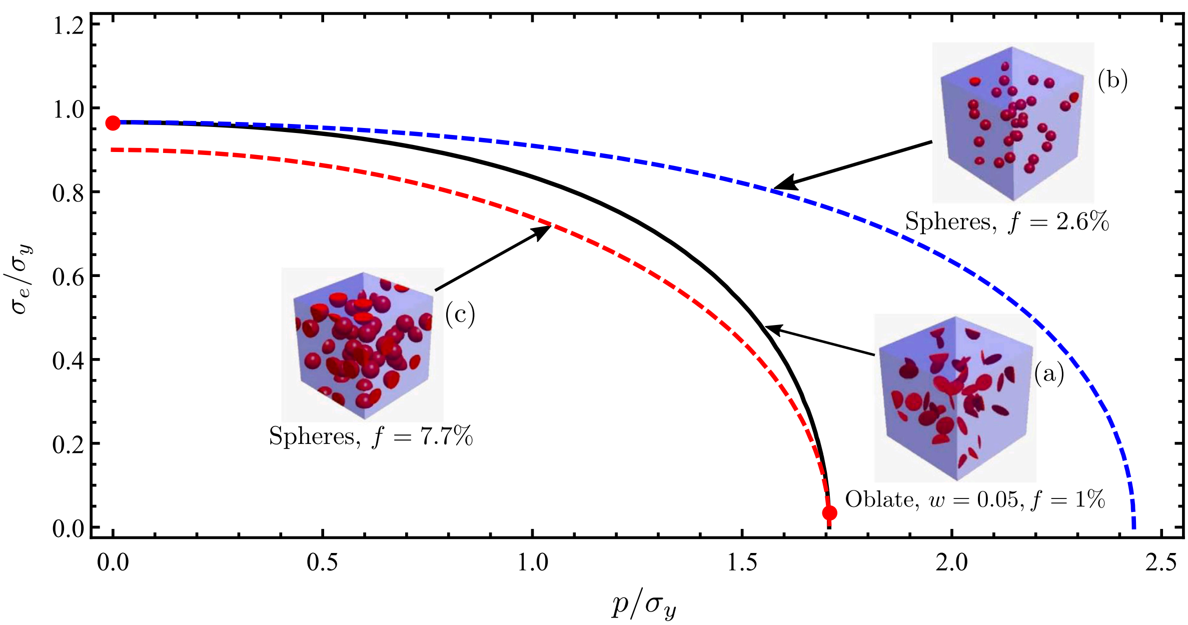

Fig. 6. Yield curves on the normalized $p - \sigma_e$ plane for a random distribution of oblate voids ($w = 0.05$) with $f = 1\%$, spherical voids at a low porosity of $f = 2.6\%$ and spherical voids at a high porosity of $f = 7.7\%$.

Fig. 5 shows the normalized hydrostatic p/σ_y and shear σ_e/σ_y points, respectively, as a function of the void aspect ratio w at three different porosity values f = 1%, 3%, and 5%. As w decreases, both the hydrostatic and shear points decrease rapidly, with the former being more sensitive to the void shape changes. Once again, this behavior confirms the non-trivial dependence of the plastic response on the void shape parameter.

Fig. 6 showcases the paramount differences between microstructures with spherical and oblate voids. More specifically, we show the yield curves for a random distribution of (a) oblate voids ($w = 0.05$) with $f = 1\%$, (b) spherical voids at a low porosity of $f = 2.6\%$, and (c) spherical voids at a high porosity of $f = 7.7\%$. In cases (b) and (c) with spherical voids, the values of porosity were chosen so that the corresponding yield surfaces have the same hydrostatic ($f = 7.7\%$) and shear points ($f = 2.6\%$) as the yield surface of the microstructure comprising oblate voids with $f = 1\%$. Comparison of the results for microstructures (a) and (b) shows that the response of a material whose microstructure consists of oblate voids is much more compliant than that with spherical voids, especially for stress states in which the hydrostatic component dominates ($p \gg \sigma_e$). On the other hand, comparison of the results for microstructures (a) and (c) shows that a material comprising a random distribution of oblate voids with $f = 1\%$ and $w = 0.05$ exhibits fairly similar behavior with a material consisting of spherical voids with approximately eight times higher porosity, i.e., $f = 7.7\%$ and $w = 1$. Such results are indicative of the fact that, even at low porosities, the existence of flat voids (the shape of which deviates considerably from spherical) can have a detrimental effect on the effective plastic response of the porous material.

We conclude this section with a parametric analysis of the effects of function $k(w)$, used in (3.12) to define the calibration function $\alpha(f, w)$, on the predictions of the model. Fig. 7 shows the influence of k on the shape and size of the yield surface and on the volumetric plastic strain-rate N_{kk}. For demonstration purposes, fixed values for the void aspect ratio ($w = 0.10$) and porosity ($f = 5\%$) are used. As the value of k increases, the hydrostatic point moves "outwards", thus making the response stiffer for stress states with $p \gg \sigma_e$, whereas the material

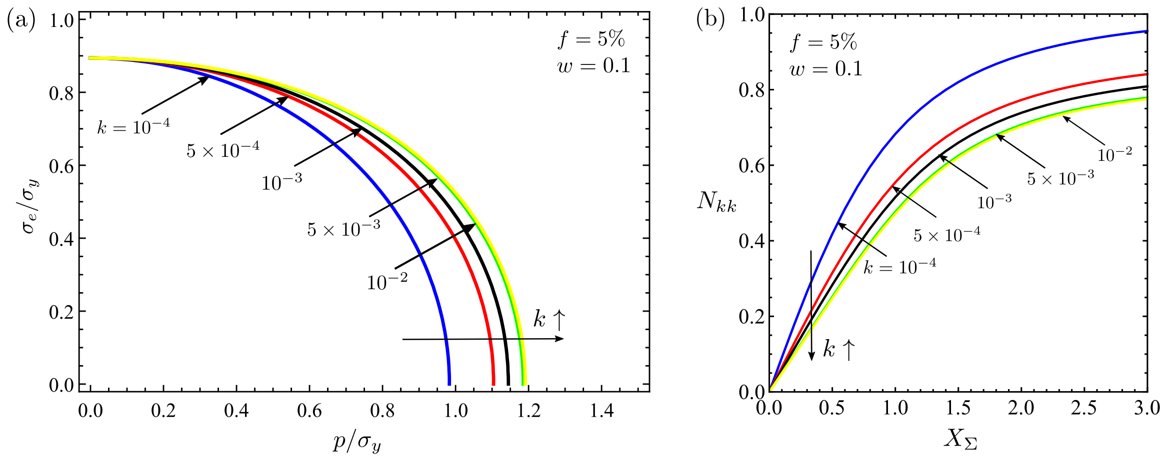

Fig. 7. Influence of parameter k on (a) the yield curve on the normalized $p - \sigma_e$ plane and (b) the variation of the normalized volumetric plastic strain-rate N_{kk} with stress triaxiality X_Σ.

response in shear is marginally affected (Fig. 7a). Accordingly, the corresponding values of N_{kk} decrease as k increases, and this leads to reduced porosity growth, especially at higher stress triaxialities. We also note that the parameter $k(w)$ does not affect the hydrostatic point when $w = 1$ (spherical voids). Also, in this special case of spherical voids ($w = 1$), the model recovers the Gurson hydrostatic point irrespective of the value of $k(1)$ and α. Nonetheless, the rate at which the yield curve approaches that point is obviously affected by α (see discussion in Mbiakop et al. (2015b)).

5. Results: Numerical RVE homogenization and model assessment

In this section, the analytical model presented in Section 3 is calibrated by comparing its predictions to the results of numerical homogenization calculations of representative volume elements (RVE). Results from finite element calculations of periodic unit cells that contain uniformly distributed and randomly orientated voids of various shapes in an isotropic matrix are presented first. To ensure accurate comparisons with the predictions of the homogenization model, assessment of the typical RVE characteristics, such as isotropy of the cells and effective behavior convergence, is carried-out.

5.1. Unit cell calculations

Concerning validation techniques at the *material (constitutive) level*, the numerical periodic homogenization method may be used as a test-bed to assess the predictions of analytical homogenization models. The methodology used herein can be summarized as follows. A suitably chosen RVE containing randomly oriented and distributed with uniform probability spheroidal voids of predefined initial volume fraction is loaded and periodic boundary conditions are applied. The finite element method is used to determine the *local*[5] displacement, strain, and stress fields in the RVE. The local fields are then used to calculate the corresponding *average* fields. The fitting parameters A, B, and f_{min} used in the interpolation function α in (3.12), are then adjusted to align the predictions of the analytical model with the average numerical results.

In this work, cubic unit cells with side lengths $L_1 = L_2 = L_3 = 1$ and initial volume $\mathcal{V}_0 = L_1 L_2 L_3 = 1$ are filled with uniform distributions of randomly oriented voids of the same spheroidal shapes and initial porosities. The unit cells are subjected to constant average stress triaxiality and Lode angle θ under periodic boundary conditions (Michel et al., 1999). Implementation of such constant stress triaxiality and Lode parameter loading conditions has been discussed extensively in the literature (e.g., Barsoum and Faleskog (2007), Dunand and Mohr (2014), Mbiakop et al. (2015b)) and for the sake of brevity they will not be repeated here; the reader is referred to Section 4.2 in Mbiakop et al. (2015b) for more details.

Using as an indicator both previous numerical results (Danas and Aravas (2012), Cao et al. (2015), Anoukou et al. (2018), Zerhouni et al. (2021)) and the results presented in Section 4, only oblate voids (i.e., $w \leq 1$) are considered, since prolate voids exhibit substantially weaker effects on the effective response. The geometry of the unit cells is generated using the Random Sequential Adsorption (RSA) method discussed in Anoukou et al. (2018). Therein, ellipsoidal voids of the same or different size are sequentially added in the unit cell imposing a non-overlapping condition based on distance evaluation of quadric objects of general shape. When the desired volume fraction (porosity) is reached, periodic images of any "incomplete" voids at the cube boundaries are added.

The matrix material is assumed to be isotropic with Young's modulus $E = 300\,\sigma_0$, Poisson's ratio $\nu = 0.3$, and a flow stress following power law isotropic hardening[6] of the form

$$\sigma_y(\bar{\varepsilon}^p) = \sigma_0 \left(1 + \frac{\bar{\varepsilon}^p}{\varepsilon_0}\right)^{1/n}, \tag{5.1}$$

is used, where $n \geq 1$ is the hardening exponent and $\varepsilon_0 = \sigma_0/E$. A hardening exponent of $n = 10$ is used in all calculations. The average porosity in the unit cell is calculated using the corresponding average deformation gradient as

$$f = \frac{\mathcal{V}^{\mathrm{v}}}{\mathcal{V}} = \frac{\det \mathbf{F} - \mathcal{V}^{\mathrm{m}}/\mathcal{V}_0}{\det \mathbf{F}}, \qquad \det \mathbf{F} = \frac{\mathcal{V}}{\mathcal{V}_0}, \qquad \mathcal{V} = \mathcal{V}^{\mathrm{m}} + \mathcal{V}^{\mathrm{v}}, \tag{5.2}$$

where $\mathcal{V}^{\mathrm{m}}$ is the current matrix volume, $\mathcal{V}^{\mathrm{v}}$ the current volume of the voids, and $\mathcal{V}$ the current total volume of the RVE.

5.1.1. Computational aspects of RVE simulations

The FE calculations are carried-out using the commercial finite element program ABAQUS/Standard (Abaqus, 2021). The power-law isotropic hardening model for the matrix material is implemented via a User HARDening (UHARD) user-subroutine provided by ABAQUS/Standard. Loading under constant stress triaxiality and Lode angle is achieved through a time-dependent nonlinear constraint, which is enforced

[5] In the context of homogenization theory, these are the fields that develop at the scale of the various heterogeneities as opposed to the (measurable) fields at the scale of the applied macroscopic loads.

[6] Any other hardening law including kinematic hardening as discussed in Cheng et al. (2017) may be used if required. This is however beyond the scope of the present study.

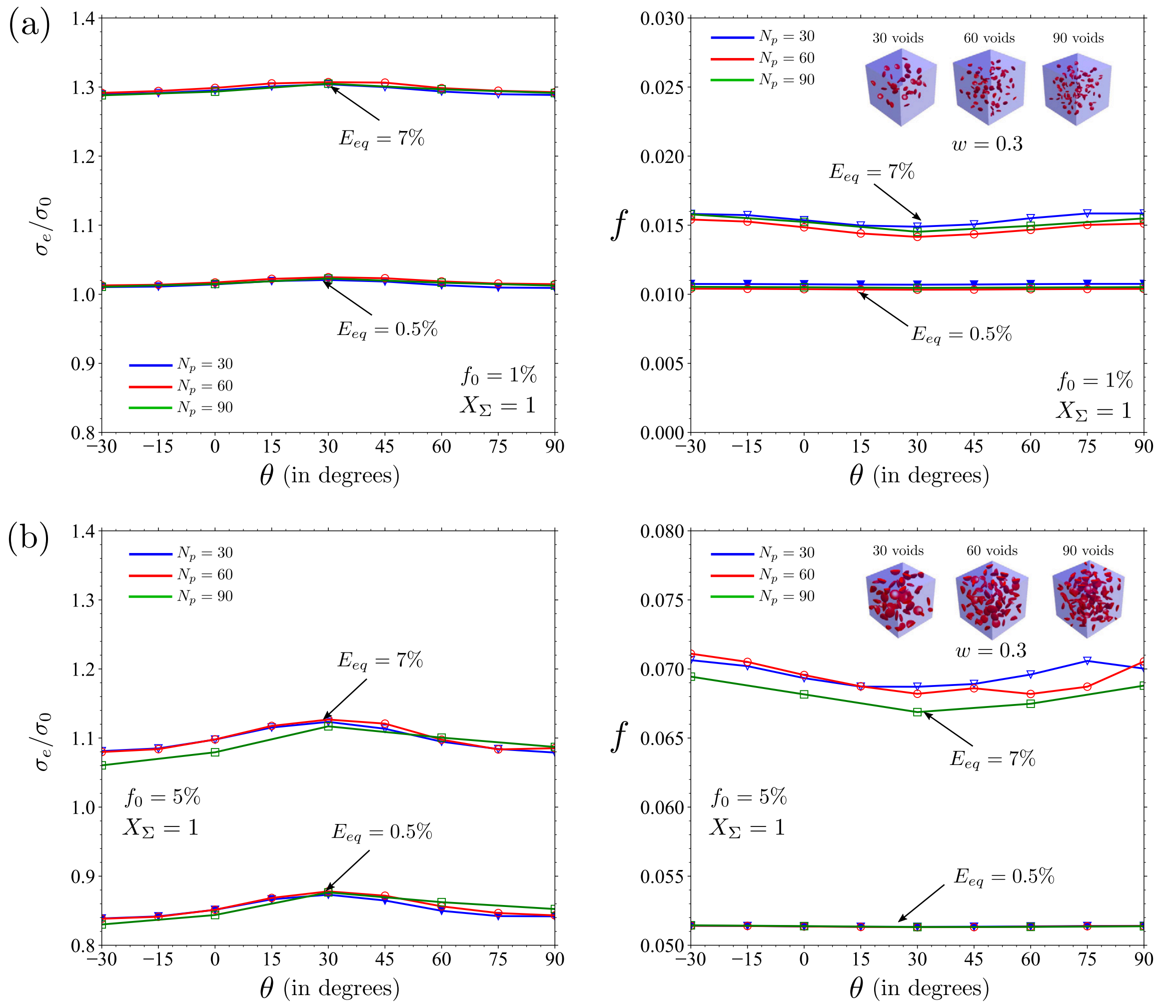

Fig. 8. Cross-plots of average normalized von Mises stress σ_{eq}/σ_0 and porosity f as functions of Lode angle θ for $w = 0.3$ and for three different number of voids (N_p = 30, 60, and 90), at an initial porosity level (a) $f_0 = 1\%$ and (b) $f_0 = 5\%$.

at every increment using the Multiple Point Constraint (MPC) user-subroutine in ABAQUS/Standard.

All meshes are generated with the mesh generation program NETGEN[7] (https://ngsolve.org). Ten-node quadratic tetrahedral hybrid elements with constant pressure (C3D10H) are used in the simulations. Mesh convergence studies of microstructures with oblate voids show that the number of required elements vary from 8.5×10^5 to 1.5×10^6, depending on the initial porosity and, more importantly, on the void shape; as the value of the aspect ratio w decreases, the number of required elements increases. It is worth noting that, in the case of spherical voids ($w = 1$), convergence of the effective behavior can be achieved with mesh densities in the range of $2{\times}10^5$ elements, depending on the value of the initial porosity; these numbers are much smaller than the number of elements required for oblate voids with an aspect ratio $w = 0.3$ for the same initial volume fractions.

The simulations are carried out using parallel computing (20 cpus per simulation) on a high-performance computing (HPC) cluster; for oblate voids with low aspect ratios ($w \le 0.5$), the average computation time per simulation ranges from 24 to 48 h depending on the mesh density. It should be pointed-out that simulations for $w \le 0.2$ could not be performed, mainly due to significant meshing quality problems. Also, based on the computational times required for $w = 0.3$, we expect very high computational times to be required for such calculations.

5.1.2. RVE determination and convergence study

It has become clear from previous (e.g. Suquet (1987), Kanit et al. (2003)) and more recent numerical homogenization studies (Lopez-Pamies et al., 2013; Benhizia et al., 2014; El Moumen et al., 2014, 2015a,b; Bensaada et al., 2022; Luo et al., 2023) on porous and particle-reinforced materials that determination of an appropriate RVE requires to investigate the convergence of the average material behavior with respect to a number of parameters in the RVE. In porous materials, these include the number of voids, different realizations of the same microstructures (different spatial distribution of voids with the same shape and volume fraction), and, for the model considered in this work, examination of the RVE's isotropy. To this end, a systematic investigation for the determination of RVE characteristics is carried-out. Unit cell calculations are performed at a constant stress triaxiality $X_\Sigma = 1$, since moderate to high triaxialities are of interest. Dependence on the Lode parameter (or equivalently the third invariant J_3 of the deviatoric stress) is examined through variation of the Lode angle θ. Results for oblate microstructures with an aspect ratio $w = 0.3$ are presented in the following. Due to severe mesh distortion issues with progressing deformation, the calculations were terminated at moderate average strain levels in this case.

Fig. 8 shows results of the convergence analysis for different *number of voids* N_p. Cross-plots for the average von Mises stress and porosity as

[7] Alternatively, it is also possible to use the open-source, 3D mesh generation software GMSH (https://gmsh.info), as discussed recently in Luo et al. (2023).

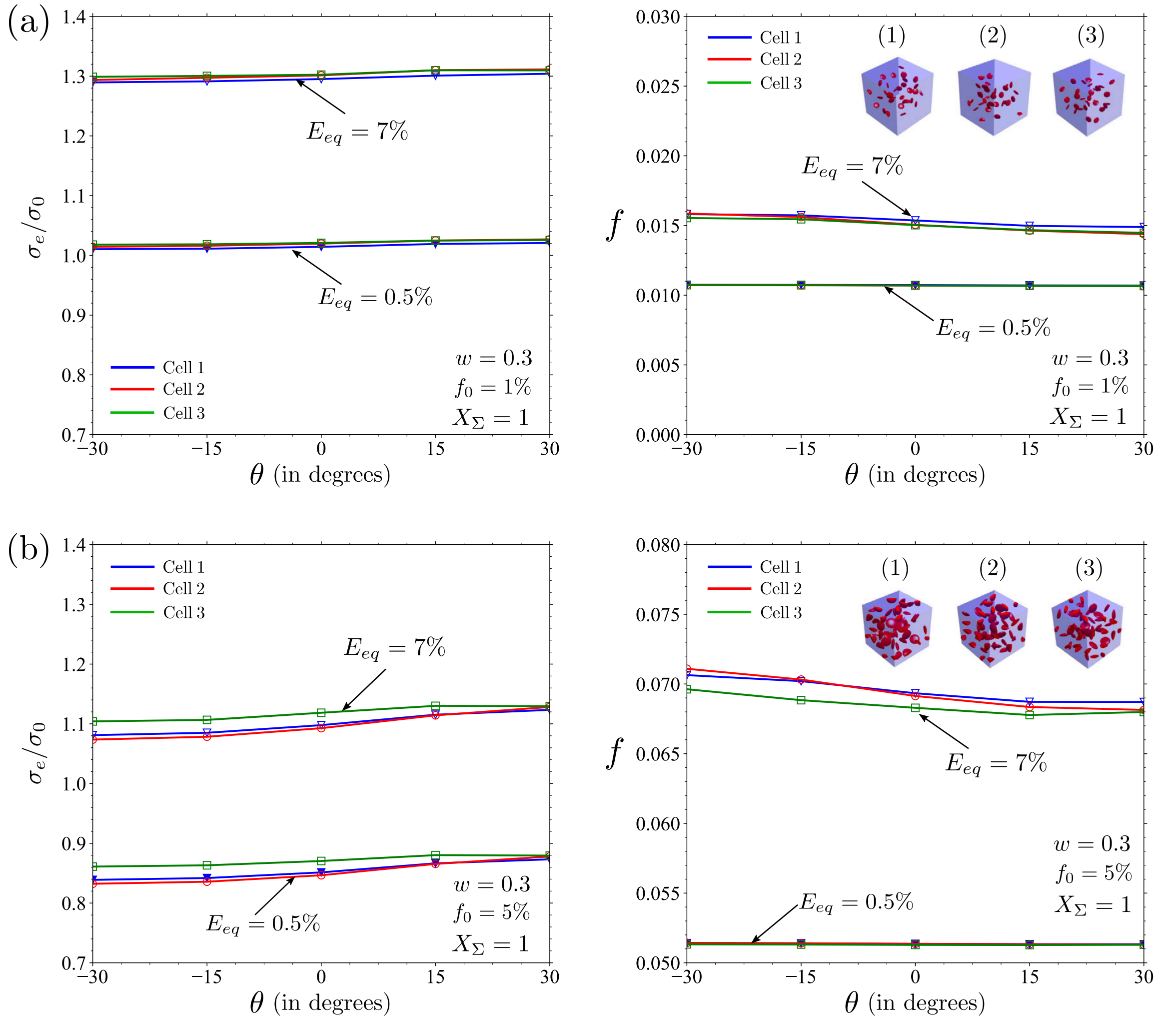

Fig. 9. Cross-plots of average normalized von Mises stress σ_{eq}/σ_0 and porosity f as functions of Lode angle θ for three different cell realizations at an initial porosity level (a) $f_0 = 1\%$ and (b) $f_0 = 5\%$.

functions of Lode angle θ (in degrees) at strain levels $E_{eq} = 0.5\%$ and 7% are presented for microstructures comprising three different void numbers ($N_p = 30$, 60, and 90). Note that the vertical axes do not start at the value of zero. A Lode angle range of $\Delta\theta = 120°$ (as opposed to 60°) was intentionally scanned in these series of calculations, to verify the validity of the material isotropy hypothesis of the unit cells. It can be seen from Fig. 8a that, for a low initial porosity $f_0 = 1\%$, the scatter in the prediction of the overall porosity evolution is small at all strain levels, leading to an almost identical behavior for the average von Mises stress for all microstructures. A qualitatively similar response is observed for the higher initial porosity of $f_0 = 5\%$ (Fig. 8b). Very good agreement can be observed in the results for the microstructures comprising $N_p = 30$ and $N_p = 60$ voids, while a small deviation exists for the microstructures with $N_p = 90$ voids; this difference is more pronounced at the larger average strain of $E_{eq} = 7\%$.

The dependence of the results on the Lode angle is rather weak, at least for the range of strains considered. Examination of the predictions for the effective von Mises stress as a function of the Lode angle[8] reveals that for all microstructures considered, there exists approximately a 60° symmetry with respect to $\theta = 30°$ with maximum differences between corresponding points being less than 2%; this indicates that the unit cells can be considered, to within this approximation, as close to isotropic and be used for a fair comparison with the analytical model.

The results depicted in Fig. 8 show that a distribution of $N_p = 30$ voids provides sufficient convergence of the effective behavior. For computational efficiency, all subsequent unit cell calculations are carried out with a number of $N_p = 30$ voids.

Fig. 9 shows the results from the convergence analysis with respect to three different realizations of the same microstructure comprising $N_p = 30$ voids. The RSA algorithm is used to generate multiple isotropic microstructures with a given initial porosity, void shape, and number of voids, but with *different spatial position* of the voids in the matrix material. Again, we present cross-plots for the average von-Mises stress and porosity as functions of the Lode angle at different levels of straining. The range of $\theta \in [-30°, 30°]$ was examined in this series of calculations. In the case of an initial porosity $f_0 = 1\%$, Fig. 9a shows a good agreement among the predictions of the three realizations at the strain levels considered. A similar behavior is observed at the higher initial porosity of $f_0 = 5\%$ (Fig. 9b). Once again, there exists only a weak variation of the effective behavior with the Lode angle.

Based on these results, it is reasonable to assume that the Lode parameter has a weak effect on the effective plastic response of a porous material especially at the smaller values of w considered here. Therefore, plasticity is assumed to be independent of the Lode angle in the present analytical model.

[8] Recall that a relation of the form $\sigma_e = \sigma_e(\theta)$ describes the corresponding yield curve on the so-called Π-plane (Danas et al., 2008b).

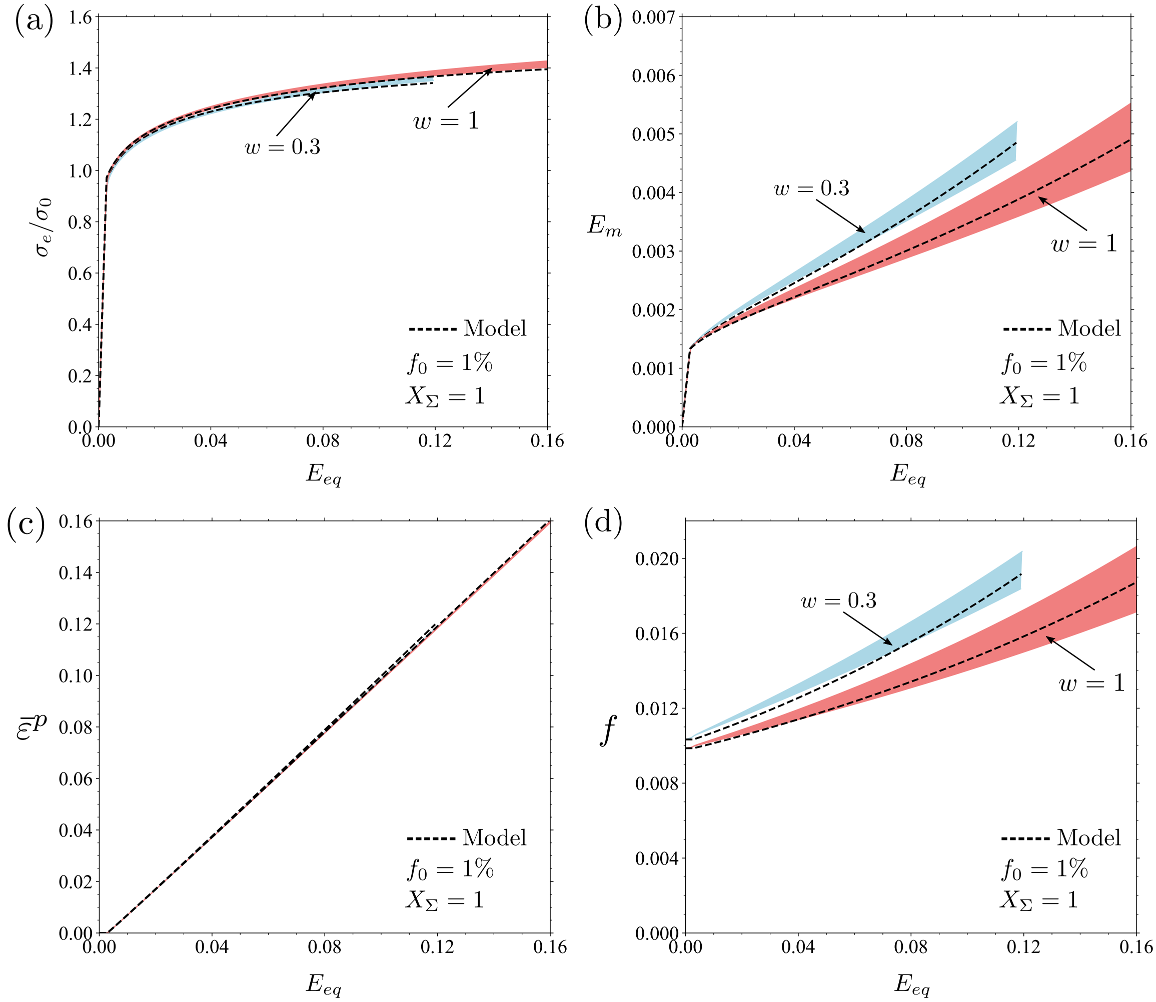

Fig. 10. Comparison of average RVE response with the corresponding predictions of the homogenization model for an initial porosity $f_0 = 1\%$ at a constant stress triaxiality $X_\Sigma = 1$. The shaded areas indicate the scatter of the RVE response over different Lode angles $\theta \in [-30°, 30°]$.

Remark 6. Nevertheless, if deemed absolutely necessary, extension of the present model to include Lode angle-dependence could be employed through various approaches. One possibility would be to include in the evolution equation of porosity (3.16) an additional term that depends on the third invariant of the stress deviator, as suggested by Nahshon and Hutchinson (2008). Another approach could be the introduction of an additional, Lode angle-dependent, shear-induced damage variable along with a corresponding evolution law as proposed by Zhou et al. (2014). Also, in the spirit of the model proposed by Bai and Wierzbicki (2008), a Lode angle dependent factor could be introduced directly into the yield function. Finally, one could of course bring the proposed isotropic projection approach in more elaborate homogenization methods (e.g., Danas and Ponte Castañeda (2009a), Agoras and Ponte Castañeda (2014), Song and Ponte Castañeda (2018)), which naturally include dependence on the Lode parameter.

5.2. Fitting between the homogenization model and average RVE response

Alignment of the analytical model with the average RVE response is achieved through variation of the fitting parameters A, B and f_{min} of the interpolation function α in (3.12). In particular, we calibrate directly those parameters by carrying out calculations with the analytical model using the same material parameters and loading conditions as in the RVE simulations. We find that the evolution of the average von Mises stress and porosity, as predicted by the analytical model, for different values of the void aspect ratio w and initial porosities, fits well the average RVE response for $A = -8.6 \times 10^{-4}$, $B = 1.06 \times 10^{-3}$ and $f_{min} = 0.005$ in Eq. (3.12).

To illustrate the variation in the effective response with the aspect ratio w, results are presented for two different microstructures: one consisting of oblate voids with aspect ratio $w = 0.3$ and another with spherical voids ($w = 1$) for an initial porosity $f_0 = 1\%$. Similar results were also obtained for an initial porosity of $f_0 = 5\%$ but are not shown here for brevity.

Figs. 10a–d show the comparison between numerical homogenization results and the predictions of the analytical model for an initial porosity of $f_0 = 1\%$ and a triaxiality $X_\Sigma = 1$. The shaded areas in Fig. 10 indicate fluctuations of the effective behavior from the unit cell calculations with respect to different values of the Lode angle in the range $\theta \in [-30°, 30°]$; blue color corresponds to oblate voids with an aspect ratio $w = 0.3$ and red color corresponds to spherical voids ($w = 1$). The black dashed curve corresponds to the predictions of the proposed analytical model, which does not have any dependence on the Lode angle. It is observed that the average hydrostatic strain shown in Fig. 10b as well as the porosity evolution shown in Fig. 10d are higher in the case of voids with an aspect ratio of $w = 0.3$ compared to a microstructure with spherical voids. The effect of higher porosity in the former case is reflected in the corresponding average stress–strain response (Fig. 10a); this effect is weak though, due the overall small porosity levels developed. It is also interesting to emphasize that the numerical and analytical results for the equivalent plastic strain in the matrix coincide and are independent of the assumed void shape (Fig. 10c).

Remark 7. Due to approximations introduced during the meshing of the voided unit cells, the resulting numerical meshed initial porosity is slightly higher ($f_0 \cong 0.0104$) for oblate voids and slightly lower ($f \cong 0.0098$) for spherical voids than the prescribed value of $f_0 = 0.010$.

We observe that the largest fluctuations in the scatter of the effective RVE response with respect to the Lode angle appear in the porosity evolution of initially spherical voids. This dependence on the Lode angle, although weak overall, becomes more important with progressing deformation, which was known from previous studies such as Danas et al. (2008b), Danas and Ponte Castañeda (2012). This may be attributed to the fact that, although both microstructures are initially isotropic, their evolution in the case of finite deformations is rather different. In the case of $w = 1$, the initially spherical voids change their shape in the same *average* way. This leads to deformation-induced anisotropic effective behavior at higher strains. On the other hand, in the case of randomly oriented spheroids, the voids are not expected to all evolve in the same manner, since deformation of each void will ultimately depend on its relative orientation with respect to the applied load. In this latter case, the microstructure is able to retain fairly well its initial isotropy, even at larger strains, showing less sensitivity to the Lode angle parameter.

Overall good agreement is achieved on average between the numerical and analytical results, both for oblate and spherical voids, up to the strain levels attained. This study shows that the proposed analytical model, together with the appropriate choice of the fitting parameters in the interpolation function introduced in (3.12), can capture well the stress and porosity evolution, when compared to full-field numerical results from RVE calculations. In any case, this comparison is not meant to be exhaustive, but it can be used to gain intuition on the effect of the void shape upon the effective response of the porous material.

6. Results: Model predictions and boundary value problem solution

In this section, we use the fitted analytical model to obtain predictions for the stress–strain response, as well as the evolution of accumulated plastic strain and porosity, for various initial void shapes under different stress states. The constitutive model has been implemented in a standard FE framework and a three-dimensional simulation of the industrially relevant quasi-static hole expansion test is performed to showcase the capabilities of the model. In the following results, a matrix material with isotropic hardening of the form (5.1) and a hardening exponent $n = 10$ is considered.

6.1. Evolution of microstructure

In order to investigate the predictions of the new model, material point (constitutive) calculations for various microstructural configurations and different stress states (defined by the stress triaxiality parameter) are carried out. We consider three different microstructures consisting of spherical voids and oblate voids with aspect ratios $w = 0.3$ and $w = 0.1$ respectively at constant low ($X_\Sigma = 1/3$) and high ($X_\Sigma = 3$) stress triaxiality. The matrix material is characterized by a Young's modulus $E = 300\,\sigma_0$ and a Poisson's ratio $\nu = 0.3$ in all calculations. Also, for comparison purposes, the same calculations are repeated using the well-known "Gurson–Tvergaard–Needleman" (GTN) model (Gurson, 1977; Chu and Needleman, 1980; Tvergaard and Needleman, 1984) with a yield function of the form:

$$\Phi^{\mathrm{GTN}}(\sigma_e, p, \bar{\varepsilon}^p, f) = \left(\frac{\sigma_e}{\sigma_y(\bar{\varepsilon}^p)}\right)^2 + 2\, f\, q_1\, \cosh\left(\frac{3\, q_2}{2}\frac{p}{\sigma_y(\bar{\varepsilon}^p)}\right) - (1 + q_3\, f^2), \tag{6.1}$$

where (q_1, q_2, q_3) are calibration parameters. For $q_1 = q_2 = q_3 = 1$, Eq. (6.1) reduces to the original Gurson's yield function. Following Tvergaard (1981), we use the values $q_1 = 1.5$, $q_2 = 1$, and $q_3 = q_1^2$ in subsequent calculations. We recall that the GTN model, originating from a modification of the Gurson model, is valid for spherical voids that remain spherical at finite strains. We show that the aspect ratio w can be viewed as a calibration parameter for the newly proposed homogenization model, similar to the aforementioned (q_1, q_2, q_3) calibration parameters in the GTN model.

In this set of calculations, σ_e and p are increased in proportion according to the desired triaxiality, and the solution is developed incrementally. Figs. 11a,b show the stress–strain response and the corresponding porosity evolution for the three different microstructures with $w = 0.1$, 0.3, and 1, and triaxialities $X_\Sigma = 1/3$ and 3. At large stress triaxiality $X_\Sigma = 3$, the effective response appears very sensitive to w and the material becomes gradually softer for lower values of the aspect ratio. Porosity evolves rapidly to extremely large values for all w, and increases faster at lower strain levels for oblate voids with smaller aspect ratios. On the other hand, at a stress triaxiality of $X_\Sigma = 1/3$, the response appears almost insensitive to the aspect ratio for spherical and oblate voids with an aspect ratio $w = 0.3$, whereas a fast increase of porosity is predicted for $w = 0.1$. The latter leads to a substantial drop in the corresponding stress–strain response as shown in Fig. 11a. This observation suggests that the initial void shape alone is a predominant variable and can induce local softening even at loads with a *small hydrostatic component*. This effect is highly nonlinear with respect to w and tends to become stronger for $w < 0.5$.

Figs. 11c,d show the evolution of the equivalent plastic strain and strain triaxiality. For a stress triaxiality of $X_\Sigma = 3$, the aspect ratio w does affect the accumulated plastic strain in the matrix, whereas this effect becomes stronger for lower values of w. Also, strain triaxiality reaches higher values at lower overall strains as the void aspect ratio decreases, thus indicating that very high dilatational strains develop for microstructures containing flat oblate voids. At a low stress triaxiality of $X_\Sigma = 1/3$, the aspect ratio does not affect the equivalent plastic strain in the matrix, whereby higher strain triaxiality is only obtained for the case of $w = 0.1$, which is consistent with the corresponding porosity evolution shown in Fig. 11b.

It is also interesting to note that the predictions of the GTN model are very close to those of the proposed new model with $w = 0.3$ in the case of the high triaxiality $X_\Sigma = 3$. In turn, at the lower triaxiality of $X_\Sigma = 1/3$, the GTN predictions are close to those of the proposed model with $w = 1$. This indicates that the proposed new model is able to reproduce such results with a variation of only one parameter (the aspect ratio w) that nevertheless incorporates a physical meaning related to the microstructure.

Figs. 12a,b showcase the effect of initial porosity on the stress–strain response and porosity evolution for the three different initial porosity distributions $f_0 = 0.05\%$, 0.1%, and 1% at a stress triaxiality $X_\Sigma = 3$. Solid lines correspond to microstructures comprising oblate voids with an aspect ratio $w = 0.1$; for reference, microstructures with the same initial volume fractions of spherical voids (i.e., with $w = 1$) are also shown with dashed lines of corresponding color. It can be seen in all cases that for initial porosities 0.05% and 0.1% porosity evolution is relatively the same while a substantial increase in the rate of porosity evolution is observed for an initial porosity $f_0 = 1\%$. As expected, softening response initiates at lower strain levels for very flat oblate voids when compared to spherical voids at the same initial void volume fraction; also, for strain levels above 5%, porosity grows to substantially higher values at corresponding strains and initial porosities for voids with $w = 0.1$. It is interesting to also note that, up to relatively small strains of 2.5%, the effective response of a material with a microstructure consisting of penny-shaped voids with $w = 0.1$ exhibits similar behavior with a material comprising spherical voids that had 20 times more initial volume fraction in the matrix; this indicates once again the strong effect of the shape parameter in accelerating porosity evolution relative to the initial porosity content.

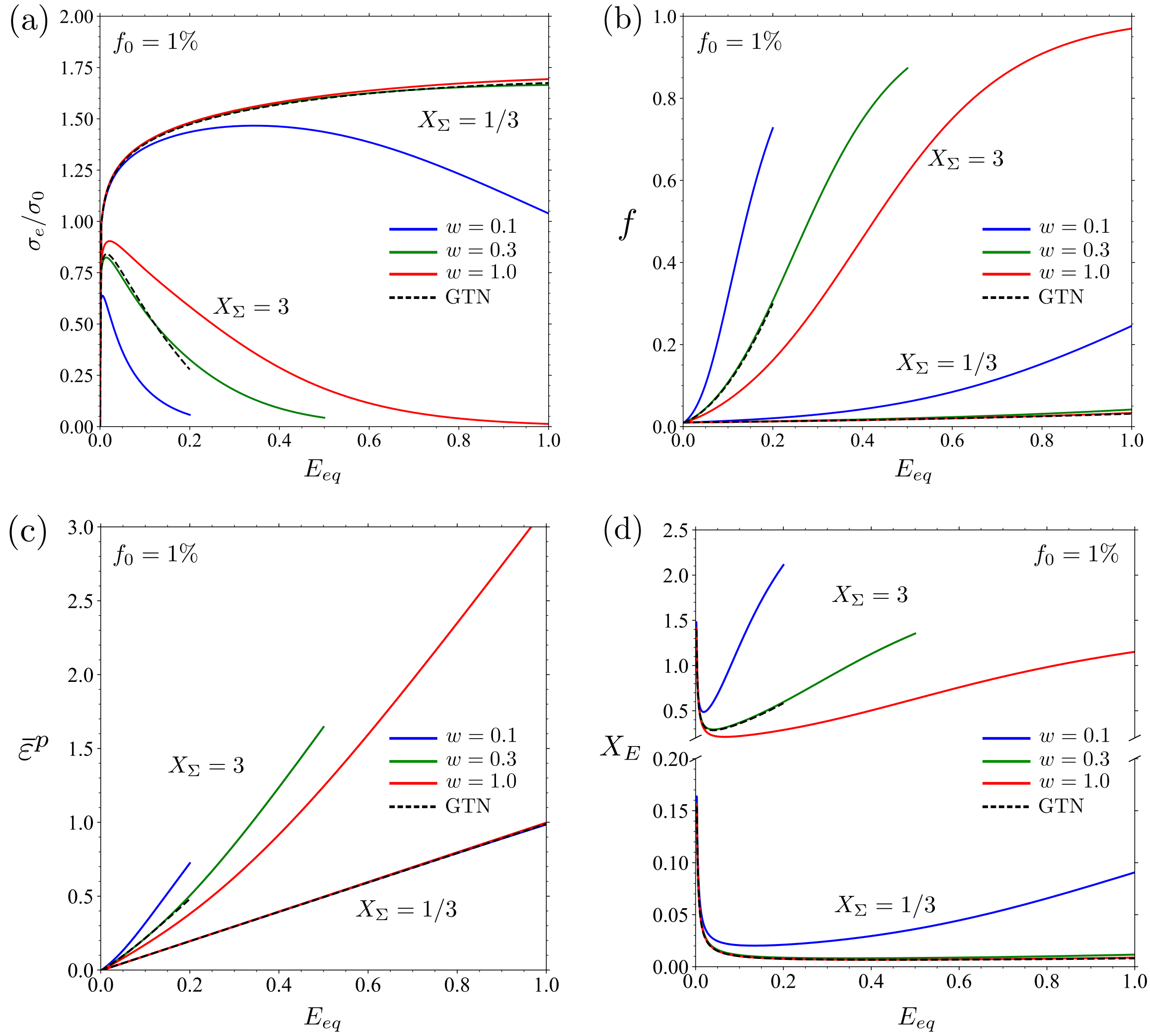

Fig. 11. Results from microstructural evolution calculations regarding the effective elastic–plastic response as predicted by the proposed homogenization model showcasing the effect of the aspect ratio parameter. Plots of (a) the normalized von Mises stress σ_e/σ_0, (b) porosity f, (c) equivalent plastic strain $\bar{\varepsilon}^p$, and (d) strain triaxiality X_E are shown for different values of the aspect ratio w both at low and high stress triaxialities. The dashed black line corresponds to the predictions of the isotropic GTN model.

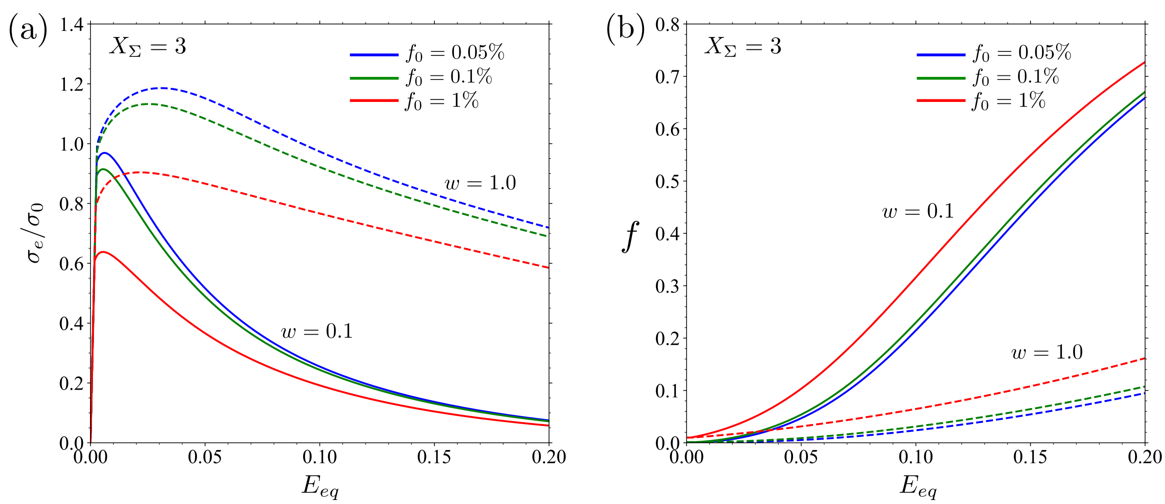

Fig. 12. Results from microstructural evolution calculations regarding the effective elastic–plastic response as predicted by the proposed model showcasing the effect of initial porosity. Plots of (a) the normalized von Mises stress σ_e/σ_0 and (b) porosity f are shown for different values of initial porosity f_0 at a high stress triaxiality $X_\Sigma = 3$. Solid lines correspond to an aspect ratio of $w = 0.1$ and dashed lines with same color correspond to respective initial porosity with $w = 1$.

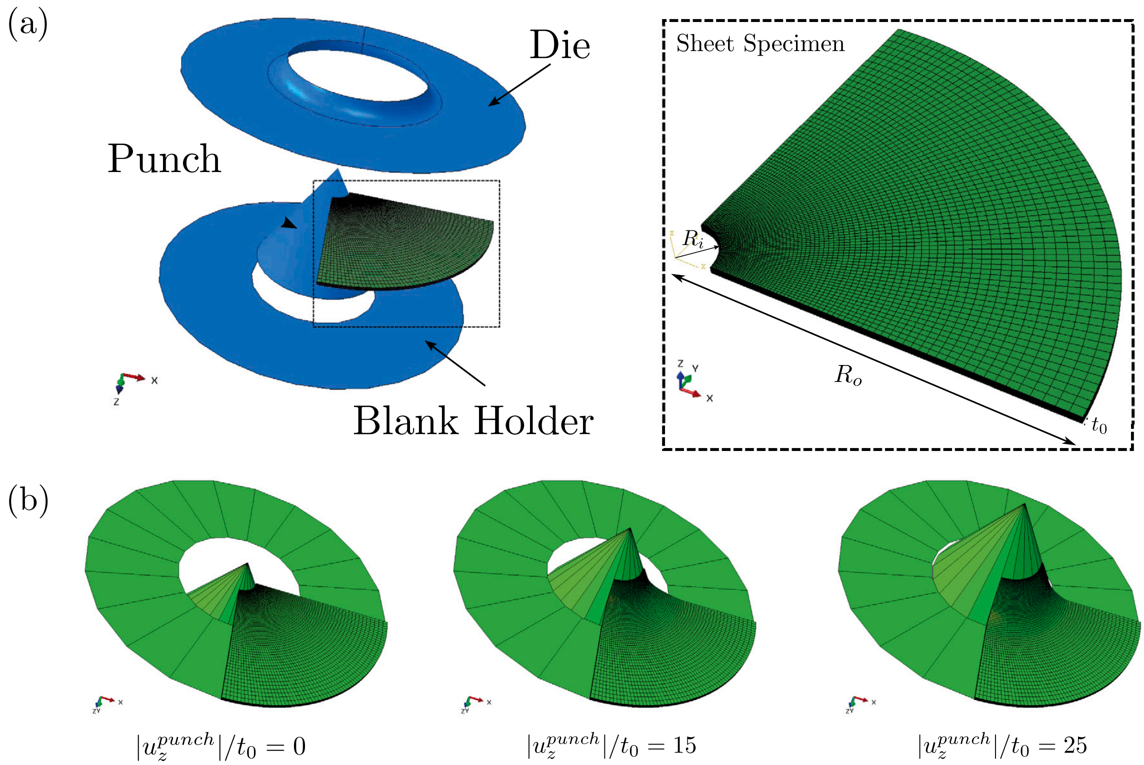

Fig. 13. (a) Simulation setup for the HET, which includes the rigid die, blank holder, and conical punch, along with a magnification of the circular specimen showing the mesh density used. (b) The deformed specimen at different stages of the forming process.

6.2. Simulation of the hole expansion test

The Hole Expansion Test (HET) (ISO 16630:2017 (2017)) is a test used widely in the steel industry for the determination of the local formability of a steel grade, using thin sheets of standardized dimensions. For the test, a hole of predefined diameter is created in a circular thin sheet specimen, which is then clamped between a die and a blank holder. Next, a conical punch of 60° apex angle expands the initial hole until a through-thickness macroscopic crack appears. The relative difference between the diameter after rupture and the initial diameter of the specimen's inner hole defines the Hole Expansion Ratio (HER), which serves as a measure of the formability (or ductility) of the steel grade.

The porous model proposed in this study has been implemented using a User MATerial subroutine (UMAT) provided by ABAQUS/Standard module allowing to numerically simulate the HET boundary value problem. Although the problem can be treated as axisymmetric, full three-dimensional simulations are intentionally performed, to demonstrate the capabilities and computational efficiency of the proposed model. The setup used for the simulations is shown in Fig. 13a. The black holder, die, and the conical punch are all modeled as rigid bodies. The circular specimen has an initial thickness t_0, an inner radius of $R_i = 5\,t_0$, and an outer radius $R_o = 50\,t_0$. To speed up the calculations, only one quarter of the whole specimen is considered and symmetry conditions are imposed. The mesh used consists of 104 720 eight-node hexahedral, hybrid elements with constant pressure (C3D8H in ABAQUS/Standard). The matrix material has a Young's modulus $E = 828\,\sigma_0$ and a Poisson's ratio $\nu = 0.3$. Two different simulations of the HET were carried out; one with a microstructure consisting of spherical voids ($w = 1$) and another with very flat voids of aspect ratio $w = 0.15$. An initial porosity of $f_0 = 1\%$ was assumed in all cases. The simulation is carried out quasi-statically in two steps. In the first step, which is used to simulate the clamping process, a displacement of $|u_z^{blank}| = 0.011\,t_0$ is imposed on the reference node of the blank holder. During the second step, the forming process is simulated by imposing a total displacement of $|u_z^{punch}| = 25\,t_0$ on the reference node of the rigid punch. The deformed state of the thin sheet during three different stages of the process is shown in 13b.

Fig. 14 shows contours of porosity f and equivalent plastic strain $\bar{\varepsilon}^p$ as predicted by the proposed homogenization model, for the two different microstructures, at the end of the corresponding simulations. Fig. 14a shows that porosity evolution is substantially larger when oblate voids with an aspect ratio $w = 0.15$ are considered, showcasing the strong effect of void shape on material response. It should be also noted that the accumulated plastic strain in the structure remains essentially the same for the two different microstructures considered (Fig. 14b). This rather interesting result is not trivial. It indicates that, the equivalent plastic strain can remain insensitive to the underlying microstructural configuration and, thus, it might not be a sufficient measure to solely characterize damage accumulation in a structure.

This can be further justified by examining the distributions of $\bar{\varepsilon}^p$ and f at a cross section of the specimen. Fig. 15a shows contour plots of $\bar{\varepsilon}^p$ and f at the end of the simulation for the case with aspect ratio $w = 0.15$. Points A and B, denoted by the red dots in the contours, are the locations of maximum porosity and equivalent plastic strain in the specimen respectively. The highest value of the plastic strain at the end of the simulation is located at the lower (inner) surface of the sheet. At that point, the specimen is in contact with the rigid punch and a compressive stress state is developed. The maximum porosity, however, appears at the upper right corner of the formed collar, which is under tension. In turn, porosity progressively decreases as one moves closer to the inner surface. Also, as shown in Fig. 15b, the evolution of $\bar{\varepsilon}^p$ and f during the forming process is quite different at points A and B. At A, porosity progressively increases to high values, while the equivalent plastic strain also increases moderately. At B, however, although the equivalent plastic strain progressively increases to higher values compared to point A, porosity rapidly decreases, since the structure is under compression at that point.

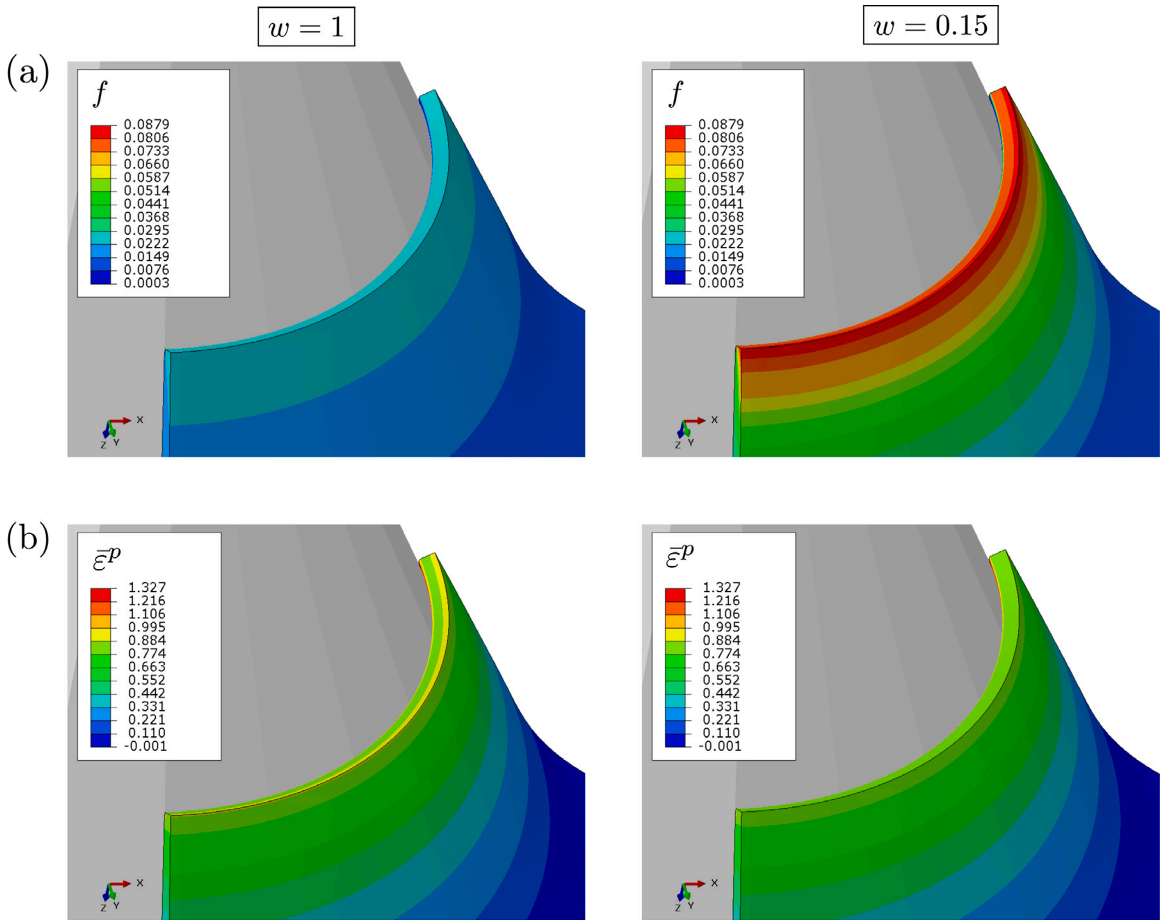

Fig. 14. Contours at the end of the analysis of (a) porosity f and (b) equivalent plastic strain $\bar{\varepsilon}^p$ for microstructures consisting of spherical voids ($w = 1$) and oblate voids with aspect ratio $w = 0.15$.

It should be recalled that, in the context of porous plasticity modeling, porosity can be viewed as a degradation (or damage) parameter for the structural load-carrying capacity. In this sense, macroscopic cracks can be identified with the regions of accumulated porosity in the structure. If a loss of stress-carrying capacity criterion was to be used in the model, based on a critical value of the porosity (e.g., Aravas and Papadioti (2021)), then, the numerical simulations predict that crack initiation would take place at the external diameter of the formed collar where porosity takes its maximum value. This prediction of the proposed model is qualitatively consistent with recent results from the experimental realization of the HET (Barlo et al. (2022)).

Such observations verify that selection of the appropriate material model is critical in structural problems involving ductile materials, where complex stress states develop. As shown with this example, standard incompressible plasticity models (such as the von Mises model) or damage models that only consider a critical value of the equivalent plastic strain in the criteria for crack initiation should be used with caution, as they might lead to inaccurate predictions. In case such models are utilized, either more information for the stress state should be included in the definition of the critical strain to failure in a phenomenological sense (e.g., Bai and Wierzbicki (2008)) or models that include more microstructural information (such as the porosity in porous elastic–plastic models) should be alternatively considered.

7. Conclusions

In this work, we propose a new rate-independent, elastic–plastic model for porous metallic materials that consist of microstructures with randomly distributed and randomly oriented spheroidal voids for the investigation of the initial void shape on the effective response of the material. In the analytical model, we assume an infinite number of void families, which are all characterized by the same shape but different orientations. The equivalence between isotropic projection and orientation averaging is utilized, resulting in a constitutive model that depends only on the shape of the voids and not their orientations. To derive a sufficiently accurate model that is simple and computationally efficient for engineering applications, we take into account porosity and matrix equivalent plastic strain evolution and assume a negligible effect of the void shape evolution during plastic flow, so that the model remains isotropic. In this manner, we are able to take into account initial void shape effects with a single parameter (the void aspect ratio w) that enters the formulation seamlessly though homogenization and characterizes the shape of the randomly oriented voids in the matrix. The model is fully explicit, resembles closely the Gurson model, and is easily implemented in standard finite element codes.

The accuracy of the analytical model is then assessed by a comparison with results from numerical homogenization. Full-field finite element calculations are carried out, using three-dimensional unit cells containing random distributions of spheroidal voids of different volume fractions and shapes, under various combinations of stress triaxiality and Lode angle. The convergence of the effective behavior with respect to the number of voids in the unit cell and different microstructural realizations is studied. We find that unit cells with as low as thirty randomly distributed and randomly oriented voids are enough to provide a behavior sufficiently close to isotropic and thus can be used as representative volume elements (RVEs) for the type of microstructures considered in this work. Sensitivity of the average RVE response with respect to the Lode angle (or equivalently to the third invariant J_3 of the

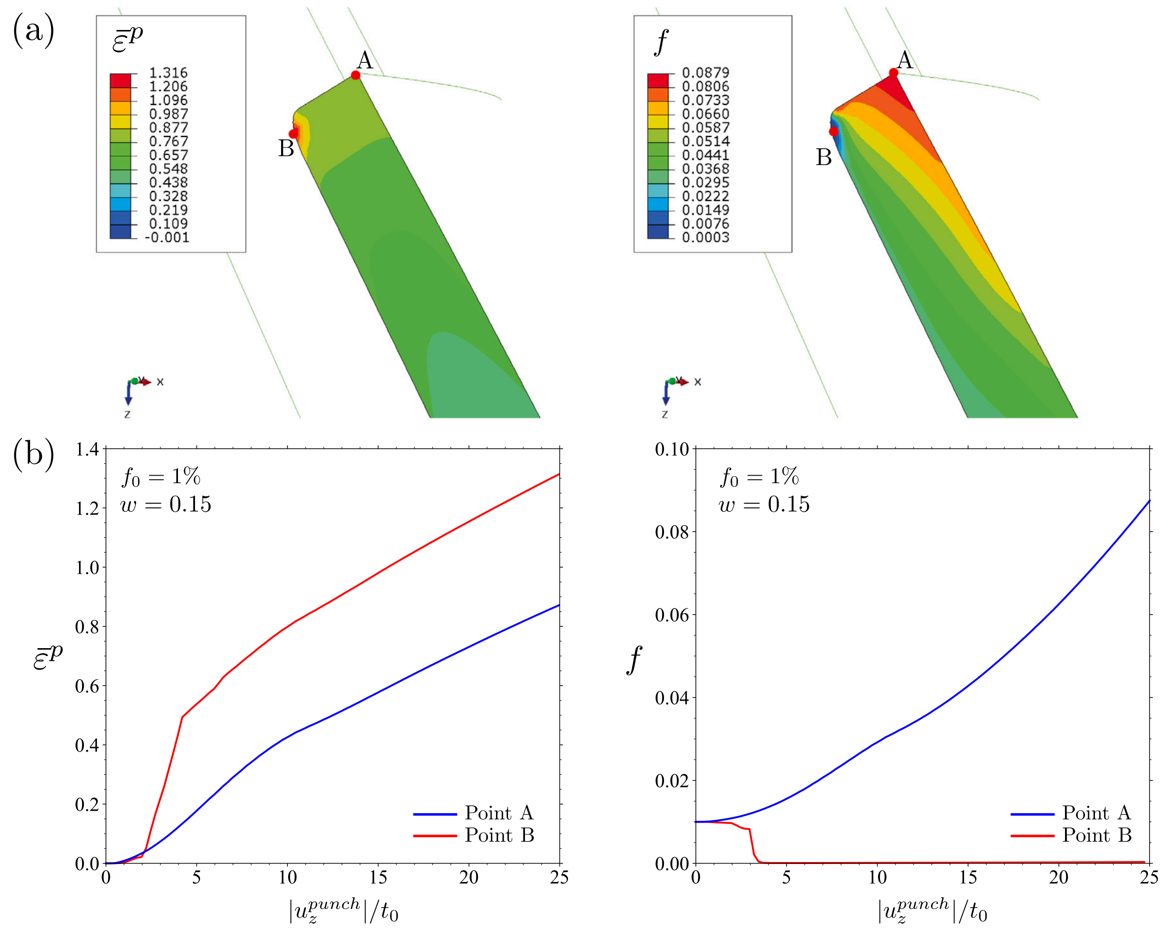

Fig. 15. (a) Distributions of the equivalent plastic strain $\bar{\varepsilon}^p$ and porosity f at a cross-section of the specimen at the end of the analysis for the case with aspect ratio $w = 0.15$. (b) Evolution of the corresponding variables during the forming process for points A and B.

deviatoric stress) is found to be relatively weak, especially at smaller values of the aspect ratio w, and thus such a dependence is not included in the analytical model. Good agreement between the average response of the RVEs and the analytical model is achieved with the introduction of only a few fitting parameters. It is also found that the average porosity evolution in unit cells containing flat-shaped voids with a low aspect ratio is greater compared to those containing spherical voids. After fitting, the model is used to investigate the effects of void shape on the homogenized elastic–plastic response of the porous material. Evolution of microstructure as predicted by the analytical model is examined both for high and moderate to low stress triaxialities, while various microstructures consisting of voids with different aspect ratios are considered. In particular, we predict rapid porosity evolution at low strain levels as the aspect ratio w takes smaller values (i.e., as the voids become more flat) resulting in significant softening. At lower stress triaxialities, a fast increase in porosity is observed for very flat penny-shaped voids ($w = 0.1$). This indicates that, even for stress states with a small hydrostatic component, the void shape effect can lead to overall softening. Also, for low stress triaxialities, the equivalent plastic strain appears to be independent of the void shape. It is also shown that the present model can reproduce the response of the well-known Gurson–Tvergaard–Needleman (GTN) model by adjusting the void aspect ratio parameter for a given stress triaxiality.

The model has been implemented in a User MATerial (UMAT) subroutine provided by ABAQUS/ Standard and the three-dimensional quasi-static hole expansion test is simulated by considering microstructures containing spherical and very flat oblate voids. This test is used in steel industry for the determination of the local formability properties of steel grades. Porosity is shown to attain much higher levels in the case of oblate voids with an aspect ratio $w = 0.15$ than for spherical voids. The distribution of equivalent plastic strain in the structure is found to be practically the same in both cases. It is also observed that the positions of maximum porosity and maximum equivalent plastic strain in the specimen do not coincide. These last two observations come to verify that criteria for loss of load-carrying capacity and crack initiation employed in continuum damage models should not solely rely on a critical value of the equivalent plastic strain, but should also take into account additional information to ensure accurate predictions.

The present model admits several possible extensions. One possibility could be to consider the limiting case of cracks, i.e., voids with aspect ratio $w \to 0$ together with porosity $f \to 0$. An analysis similar to that used by Willis (Willis, 1977, 1980, 1981) could be used to derive estimates for porous materials with randomly oriented cracks. The present model may also be extended in the context of rate-dependent viscoplasticity, either via the inclusion of strain-rate effects in the yield stress or by considering the viscoplastic version of the LCC homogenization method (Idiart and Ponte Castañeda, 2007; Danas et al., 2008b) or the approach proposed in Leblond et al. (1994). In that case one should be careful on how to include the interpolation function introduced in Eq. (3.12). In addition, given that the present porous model is very similar to Gurson's (and its extensions), one could extent it in a straightforward manner to include terms related to void nucleation such as those presented in Benzerga et al. (2016) and Lode-dependent porosity evolution similar to that presented in Nahshon and Hutchinson (2008). Finally, in order to deal with the well-known problem of mesh-dependent solutions in the finite element implementation of rate-independent softening materials, a "regularized" version of the model could be developed (Bergo et al., 2021; Tuhami et al., 2022; Wang and Faleskog, 2023). In particular, one may augment the present model by using an "implicit" non-local formulation to include porosity gradient effects as described in the recent works of Aravas and Papadioti (2021) and Aravas and Xenos (2023). Such an extension is to be addressed in the near future.

CRediT authorship contribution statement

S. Xenos: Formal analysis, Investigation, Methodology, Software, Validation, Writing – original draft, Writing – review & editing, Visualization. **N. Aravas:** Methodology, Project administration, Resources, Supervision, Writing – review & editing, Funding acquisition. **K. Danas:** Conceptualization, Funding acquisition, Investigation, Methodology, Project administration, Resources, Software, Supervision, Writing – review & editing.

Declaration of competing interest

The authors declare the following financial interests/personal relationships which may be considered as potential competing interests: Kostas Danas reports financial support was provided by European Research Council. Nikolaos Aravas reports financial support was provided by European Commission.

Data availability

Data will be made available on request.

Acknowledgments

SX would like to thank the Laboratoire de Mécanique des Solides (LMS) of École Polytechnique for partial financial support. NA acknowledges support from the Greek government and the Europen Commission through project RFCS-2015 709711. KD acknowledges support from the European Research Council (ERC) under the European Union's Horizon 2020 research and innovation program (Grant-No. 101081821).

Appendix A. Explicit expressions for the components of $\mathcal{Q}$ as a function of w

In the general case of an isotropic matrix phase and ellipsoidal voids with semi-axes a_1, a_2, a_3 (with $a_1 \geq a_2 \geq a_3$), one may derive explicit expressions for the corresponding components of the microstructural tensor $\boldsymbol{Q}$ with respect to a local system defined by the principal axes of the ellipsoids (i.e., defined by the unit vectors $\mathbf{n}^{(i)}$, $i = 1, 2, 3$). These expressions are semi-analytical, involve the numerical computation of elliptic integrals, and can be found in Mura (1987) (see also Appendix A of Aravas and Ponte Castañeda (2004)). For the special case of *spheroidal* voids (where $a_1 = a_2 = a$ and $a_3 \neq a_1, a_2$), explicit analytical expressions were derived by Cao et al. (2015), but as functions of the semi-axes defining the voids shape. However, since the model proposed in this work admits the aspect ratio $w = a_3/a_1 = a_3/a_2 = a_3/a$ as the parameter that defines the void shape, it is desirable to have the components of $\boldsymbol{Q}$ as functions of w. A simple reformulation of the expressions presented in the aforementioned work was carried out and the results are summarized below.

The expressions for the components $\mathcal{Q}_{ijkl}$ given in the following are with respect to the local coordinates system defined by the $\mathbf{n}^{(i)}$'s. The non-zero components of the microstructural tensor are given as functions of w by

$$\mathcal{Q}_{1111}(\nu_m, w) = \frac{1}{2\pi(1-\nu_m)}\left(4\pi - \frac{1}{2}I_1 - J_{11}\right), \tag{A.1}$$

$$\mathcal{Q}_{2222}(\nu_m, w) = \frac{1}{2\pi(1-\nu_m)}\left(4\pi - \frac{1}{2}I_2 - J_{22}\right), \tag{A.2}$$

$$\mathcal{Q}_{3333}(\nu_m, w) = \frac{1}{2\pi(1-\nu_m)}\left(4\pi - \frac{1}{2}I_3 - J_{33}\right), \tag{A.3}$$

$$\mathcal{Q}_{1112}(\nu_m, w) = \frac{1}{8\pi(1-\nu_m)}\left[16\pi\,\nu_m + (1-4\nu)(I_1+I_2) - J_{12}\right], \tag{A.4}$$

$$\mathcal{Q}_{1113}(\nu_m, w) = \frac{1}{8\pi(1-\nu_m)}\left[16\pi\,\nu_m + (1-4\nu)(I_1+I_3) - J_{13}\right], \tag{A.5}$$

$$\mathcal{Q}_{2233}(\nu_m, w) = \frac{1}{8\pi(1-\nu_m)}\left[16\pi\,\nu_m + (1-4\nu)(I_2+I_3) - J_{23}\right], \tag{A.6}$$

$$\mathcal{Q}_{1212}(\nu_m, w) = 1 - \frac{1}{8\pi(1-\nu_m)}\left[(1-2\nu_m)(I_1+I_2) + J_{12}\right], \tag{A.7}$$

$$\mathcal{Q}_{1313}(\nu_m, w) = 1 - \frac{1}{8\pi(1-\nu_m)}\left[(1-2\nu_m)(I_1+I_3) + J_{13}\right], \tag{A.8}$$

$$\mathcal{Q}_{2323}(\nu_m, w) = 1 - \frac{1}{8\pi(1-\nu_m)}\left[(1-2\nu_m)(I_2+I_3) + J_{23}\right], \tag{A.9}$$

where ν_m is the Poisson's ratio of the matrix material and is set to $\nu_m = 1/2$ for the plasticity case. The above coefficients are given by

- oblate voids ($0 < w < 1$):

$$I_1 = I_2 = \frac{2\pi w}{(1-w^2)^{3/2}}\left[\cos^{-1}(w) - w(1-w^2)^{1/2}\right], \quad I_3 = 4\pi - 2I_2 \tag{A.10}$$

$$J_{11} = \frac{3}{2}\left(\pi - \frac{1}{4}\frac{I_3 - I_1}{1-w^2}\right), \quad J_{22} = J_{11}, \quad J_{33} = 2\pi - \frac{w^2}{1-w^2}(I_3 - I_1), \tag{A.11}$$

$$J_{12} = 2\pi - \frac{1}{2}\frac{I_3 - I_1}{1-w^2}, \quad J_{13} = \frac{1+w^2}{1-w^2}(I_3 - I_1), \quad J_{23} = J_{13} \tag{A.12}$$

- prolate voids ($w > 1$):

$$I_1 = I_2 = \frac{2\pi w}{(w^2-1)^{3/2}}\left[w(w^2-1)^{1/2} - \cosh^{-1}(w)\right], \quad I_3 = 4\pi - 2I_2 \tag{A.13}$$

$$J_{11} = \frac{3}{2}\left(\pi - \frac{1}{4}\frac{I_2 - I_3}{w^2-1}\right), \quad J_{22} = J_{11}, \quad J_{33} = 2\pi - \frac{w^2}{w^2-1}(I_2 - I_3), \tag{A.14}$$

$$J_{12} = 2\pi - \frac{1}{2}\frac{I_2 - I_3}{w^2-1}, \quad J_{13} = \frac{w^2+1}{w^2-1}(I_2 - I_3), \quad J_{23} = J_{13} \tag{A.15}$$

- spherical voids ($w = 1$):

$$I_1 = I_2 = I_3 = \frac{4\pi}{3}, \tag{A.16}$$

$$J_{11} = J_{22} = J_{33} = \frac{6\pi}{5}, \tag{A.17}$$

$$J_{12} = J_{13} = J_{23} = \frac{8\pi}{5}. \tag{A.18}$$

The remaining non-zero components are determined by using the minor and major symmetries of $\boldsymbol{Q}$.

Appendix B. On the equivalence between isotropic projection and orientation averaging

In this Appendix, we show that the projection operation in the isotropic space, which is used in Section 3, is equivalent to averaging over all possible orientations, provided the fourth-order tensor to be projected possess the minor symmetries. The proof is as follows.

Let $A'_{\kappa_1\kappa_2\cdots\kappa_n}$ be the components of a nth-order tensor of *even* rank with respect to a local coordinate system (e.g., a system which is defined by the orientation vectors $\mathbf{n}^{(i)}$ of the principal axes of the voids) and $A_{\lambda_1\lambda_2\cdots\lambda_n}$ the components of the tensor with respect to a global (fixed) coordinate system. Then, the components with respect to the fixed system can be related to the components of the local system through the corresponding direction cosines $Q_{\kappa_i\lambda_i}$, i.e.,

$$A_{\kappa_1\kappa_2\cdots\kappa_n} = Q_{\kappa_1\lambda_1}Q_{\kappa_2\lambda_2}\cdots Q_{\kappa_n\lambda_n}A'_{\lambda_1\lambda_2\cdots\lambda_n}. \tag{B.1}$$

The direction cosines $Q_{\kappa_i\lambda_i}$ can be expressed in terms of three Euler angles (θ, ϕ, ψ), so that the orientation average of a tensor can be calculated as an average over (θ, ϕ, ψ) (e.g., Andrews (2004))[9]:

$$\langle A_{\kappa_1\kappa_2\cdots\kappa_n}\rangle = \underbrace{\frac{1}{8\pi^2}\int_{\psi=0}^{2\pi}\left[\int_{\phi=0}^{2\pi}\left(\int_{\theta=0}^{\pi} Q_{\kappa_1\lambda_1}Q_{\kappa_2\lambda_2}\cdots Q_{\kappa_n\lambda_n}\sin\theta\, d\theta\right)d\phi\right]d\psi}_{=I_{\kappa_1\kappa_2\cdots\kappa_n|\lambda_1\lambda_2\cdots\lambda_n}\equiv I^{(n)}} A'_{\lambda_1\lambda_2\cdots\lambda_n}, \tag{B.2}$$

where $I^{(n)}$ is the rotational average of the direction cosines and can be thought of as an orientation averaging operator acting on an nth-order tensor. By making use of Weyl's theorem (Weyl, 1946), it can be shown that $I^{(n)}$ can be expressed as the sum of Q_n linearly independent isotropic tensors of order n, i.e., it will be of the form (Andrews and Thirunamachandran, 1977)

$$I^{(n)} = \underset{1\times Q_n}{\lfloor f^{(n)}\rfloor}\underset{Q_n\times Q_n}{\left[M^{(n)}\right]}\underset{Q_n\times 1}{\{g^{(n)}\}}, \qquad Q_n = \sum_{r=0}^{n/2}\frac{n!(3r-n+1)}{(n-2r)!r!(r+1)!}, \tag{B.3}$$

where $\{f^{(n)}\}$ and $\{g^{(n)}\}$ are sets containing the components of linearly independent tensors of order n with respect to the fixed and the material coordinate systems respectively and $\left[M^{(n)}\right]$ is a coefficients matrix which can be calculated as

$$\underset{Q_n\times Q_n}{\left[M^{(n)}\right]} = \underset{Q_n\times Q_n}{\left[S^{(n)}\right]^{-1}}, \qquad \underset{Q_n\times Q_n}{\left[S^{(n)}\right]} = \underset{Q_n\times 1}{\{f^{(n)}\}}\underset{1\times Q_n}{\lfloor f^{(n)}\rfloor} = \underset{Q_n\times 1}{\{g^{(n)}\}}\underset{1\times Q_n}{\lfloor g^{(n)}\rfloor}, \tag{B.4}$$

under the assumption that $\left[S^{(n)}\right]$ is invertible. For even ranked tensors, each element of the aforementioned sets is a product of Kronecker deltas comprising $n/2$ factors (i.e., they are of the form $\delta_{\kappa_1\kappa_2}\cdots\delta_{\kappa_{n-1}\kappa_n}$). In the special case of fourth-order tensors (i.e., $n = 4$, $\{\kappa_1,\kappa_2,\kappa_3,\kappa_4\}\to\{i,j,k,l\}$, $\{\lambda_1,\lambda_2,\lambda_3,\lambda_4\}\to\{p,q,r,s\}$), it follows from (B.3)$_2$ that $Q_4 = 3$ and the expressions for the quantities $\{f^{(n)}\}$, $\{g^{(n)}\}$ and $\left[S^{(n)}\right]$ read

$$\underset{3\times 1}{\{f^{(4)}\}} = \begin{Bmatrix}\delta_{ij}\delta_{kl}\\ \delta_{ik}\delta_{jl}\\ \delta_{il}\delta_{jk}\end{Bmatrix}, \qquad \underset{3\times 1}{\{g^{(4)}\}} = \begin{Bmatrix}\delta_{pq}\delta_{rs}\\ \delta_{pr}\delta_{qs}\\ \delta_{ps}\delta_{qr}\end{Bmatrix}, \qquad \underset{3\times 3}{\left[S^{(4)}\right]} = \begin{bmatrix}9 & 3 & 3\\ 3 & 9 & 3\\ 3 & 3 & 9\end{bmatrix} \tag{B.5}$$

From (B.3)–(B.5), after some lengthy but straightforward calculations, one ends up with the following expression

$$I^{(4)} \equiv \mathbb{I}_{ijklpqrs} = \mathbb{O}_{ijklpqrs} + \mathbb{S}^a_{ijklpqrs}, \tag{B.6}$$

$$\mathbb{O} \equiv \mathbb{P}\mathrm{roj}_{\{\mathcal{K},\mathcal{J}\}}, \qquad \mathbb{S}^a_{ijklpqrs} = \frac{1}{12}(\delta_{il}\delta_{jk}-\delta_{ik}\delta_{jl})(\delta_{ps}\delta_{qr}-\delta_{pr}\delta_{qs}), \tag{B.7}$$

where the isotropic projection tensor $\mathbb{P}\mathrm{roj}_{\{\mathcal{K},\mathcal{J}\}}$ is defined in (3.5). Substitution of (B.6) into (B.2) yields

$$\langle \mathcal{A}_{ijkl}\rangle = \mathbb{I}_{ijklpqrs}\mathcal{A}'_{pqrs} = \mathbb{O}_{ijklpqrs}\mathcal{A}'_{pqrs} + \mathbb{S}^a_{ijklpqrs}\mathcal{A}'_{pqrs}. \tag{B.8}$$

If the fourth-order tensor $\mathcal{A}$ possesses the *minor* symmetries, using (B.7)$_2$ one can show that the second term in (B.8) vanishes, so that

$$\langle \mathcal{A}_{ijkl}\rangle = \mathbb{O}_{ijklpqrs}\mathcal{A}'_{pqrs}, \tag{B.9}$$

i.e., orientation averaging of $\mathcal{A}$ equals its projection on the space of fourth-order symmetric isotropic tensors.

Appendix C. Derivation of the yield function for the isotropic projection model

The yield criterion of the variational LCC method (see Kailasam et al. (1997), Aravas and Ponte Castañeda (2004)) takes the form

$$\frac{\boldsymbol{\sigma} : m^{\mathrm{w}} : \boldsymbol{\sigma}}{1-f} - \sigma_y^2 = 0, \tag{C.1}$$

where m^{w} is the effective microstructural fourth-order tensor (anisotropic and compressible in general) defined in (3.11). It is worth noting that when $f = 0$, the above criterion becomes identically that of J_2 plasticity.

In the present model, the microstructural tensor m^{w} is simply replaced by its isotropic projection m, which reads

$$m = \mathbb{P}\mathrm{roj}_{\{\mathcal{K},\mathcal{J}\}} :: m^{\mathrm{w}} = \frac{1}{2\,m_{\mathcal{K}}}\mathcal{K} + \frac{1}{3\,m_{\mathcal{J}}}\mathcal{J}.$$

By performing the algebra, one obtains the two shear and bulk coefficients given in (3.10), i.e.,

$$\frac{1}{3\,m_{\mathcal{J}}(f,w)} = \frac{m^{\mathrm{w}}_{ijkl}\mathcal{J}_{ijkl}}{\mathcal{J}_{mnpq}\mathcal{J}_{mnpq}} = \frac{1}{3}m^{\mathrm{w}}_{iijj}, \tag{C.2}$$

$$\frac{1}{2\,m_{\mathcal{K}}(f,w)} = \frac{m^{\mathrm{w}}_{ijkl}\mathcal{K}_{ijkl}}{\mathcal{K}_{mnpq}\mathcal{K}_{mnpq}} = \frac{1}{5}\left(m^{\mathrm{w}}_{ijij} - \frac{1}{3m_{\mathcal{J}}}\right). \tag{C.3}$$

Next, the expression (C.1) for the yield criterion may be expanded directly in terms of the von Mises equivalent stress and the hydrostatic stress to take the form

$$\frac{1}{1-f}\left(\frac{\sigma_e^2}{3\,m_{\mathcal{K}}} + \frac{p^2}{m_{\mathcal{J}}}\right) - \sigma_y^2 = 0. \tag{C.4}$$

Since the latter result is derived from the corresponding estimate of the variational method, the new estimate for the present isotropic projection model inherits the significantly stiff response for the nonlinear behavior in the case of isotropic matrix and hydrostatic loadings when compared to numerical calculations of representative volume elements (RVEs) (Michel and Suquet, 1992). To improve upon this behavior, following Danas and Aravas (2012) and Mbiakop et al. (2015b), we introduce the correction factor $q_{\mathcal{J}}^2$ in the second term (hydrostatic part) of (C.4), such that

$$\frac{1}{3\,m_{\mathcal{K}}}\left(\frac{\sigma_e}{\sigma_y}\right)^2 + q_{\mathcal{J}}^2\frac{4}{9\,m_{\mathcal{J}}}\left(\frac{3\,p}{2\,\sigma_y}\right)^2 - (1-f) = 0, \qquad q_{\mathcal{J}} = \frac{1-f}{\sqrt{f}\,\ln\frac{1}{f}}. \tag{C.5}$$

The value of the correction factor $q_{\mathcal{J}}$ is such that the exact response is recovered for purely hydrostatic loadings and spherical voids ($w = 1$) (Danas et al., 2008b) or for cylindrical voids with circular cross-section ($w \to \infty$) (Danas et al., 2008a; Mbiakop et al., 2015a). Specifically, in the case of spherical voids, one has (Bele et al., 2017)

$$m_{\mathcal{K}}(f) = \frac{1-f}{3+2\,f}, \qquad m_{\mathcal{J}}(f) = \frac{4(1-f)}{9\,f}.$$

and for purely hydrostatic loading (i.e., $\sigma_e = 0$), the required pressure for yielding is

$$\frac{|p|}{\sigma_y} = \frac{2}{3}\ln\frac{1}{f},$$

a value consistent with the corresponding prediction of the Gurson model and the rigorous bound of Ponte Castañeda (2012). Expression (C.4) is expected to give fairly accurate results at high stress triaxialities and moderate to high porosities. At low porosities and for spherical voids, earlier studies (Cao et al., 2015) have found that porosity f exhibits an exponential dependence on the hydrostatic stress p. To obtain such a dependence, one may consider the Taylor expansion of $\cosh x$ and ignore higher order terms, i.e.,

$$\cosh\left(\frac{3\,p}{2\,\sigma_y}\right) = 1 + \frac{1}{2}\left(\frac{3\,p}{2\,\sigma_y}\right)^2 + O\left[\left(\frac{3\,p}{2\,\sigma_y}\right)^4\right] \quad \text{or}$$

$$\left(\frac{3\,p}{2\,\sigma_y}\right)^2 \cong 2\left[\cosh\left(\frac{3\,p}{2\,\sigma_y}\right) - 1\right]. \tag{C.6}$$

Finally, driven by numerical results and the fact that porosity, even if it starts at low values, may eventually evolve to larger ones, we

[9] The angles ϕ and θ define the location of one of the global axes with respect to the local system and the angle ψ defines the orientation of the other two global axes. Averaging is carried out over a unit sphere, to cover all possible (ϕ,θ) orientations, and over ψ.

substitute the quadratic pressure term in (C.5) by a linear combination of $\left(3\,p/(2\,\sigma_y)\right)^2$ and the right-hand-side of $(C.6)_2$ to arrive at the final form of the yield function in Eq. (3.9). This combination of terms allows to have a fairly accurate description at small, moderate and larger porosities, which is necessary in high triaxiality loads where porosity can evolve significantly during the deformation process.

References

Abaqus, 2021. CAE/2021. Simulia, RI, USA.

Agoras, M., Ponte Castañeda, P., 2013. Iterated linear comparison bounds for viscoplastic porous materials with ellipsoidal microstructures. J. Mech. Phys. Solids 61, 701–725. http://dx.doi.org/10.1016/j.jmps.2012.11.003, URL https://www.sciencedirect.com/science/article/pii/S0022509612002414.

Agoras, M., Ponte Castañeda, P., 2014. Anisotropic finite-strain models for porous viscoplastic materials with microstructure evolution. Int. J. Solids Struct. 51, 981–1002. http://dx.doi.org/10.1016/j.ijsolstr.2013.11.025, URL https://www.sciencedirect.com/science/article/pii/S002076831300468X.

Anderson, P.M., Fleck, N.A., Johnson, K.L., 1990. Localization of plastic deformation in shear due to microcracks. J. Mech. Phys. Solids 38, 681–699. http://dx.doi.org/10.1016/0022-5096(90)90028-3, URL https://www.sciencedirect.com/science/article/pii/0022509690900283.

Andrews, S.S., 2004. Using rotational averaging to calculate the bulk response of isotropic and anisotropic samples from molecular parameters. J. Chem. Educ. 81 (877), http://dx.doi.org/10.1021/ed081p877.

Andrews, D.L., Thirunamachandran, T., 1977. On three-dimensional rotational averages. J. Chem. Phys. 67, 5026–5033. http://dx.doi.org/10.1063/1.434725.

Anoukou, K., Brenner, R., Hong, F., Pellerin, M., Danas, K., 2018. Random distribution of polydisperse ellipsoidal inclusions and homogenization estimates for porous elastic materials. Comput. Struct. 210, 87–101. http://dx.doi.org/10.1016/j.compstruc.2018.08.006, URL https://www.sciencedirect.com/science/article/pii/S0045794918304565.

Aravas, N., 1987. On the numerical integration of a class of pressure-dependent plasticity models. Internat. J. Numer. Methods Engrg. 24, 1395–1416. http://dx.doi.org/10.1002/nme.1620240713, URL https://onlinelibrary.wiley.com/doi/abs/10.1002/nme.1620240713, arXiv:https://onlinelibrary.wiley.com/doi/pdf/10.1002/nme.1620240713.

Aravas, N., Papadioti, I., 2021. A non-local plasticity model for porous metals with deformation-induced anisotropy: Mathematical and computational issues. J. Mech. Phys. Solids 146, 104190. http://dx.doi.org/10.1016/j.jmps.2020.104190, URL https://www.sciencedirect.com/science/article/pii/S0022509620304154.

Aravas, N., Ponte Castañeda, P., 2004. Numerical methods for porous metals with deformation-induced anisotropy. Comput. Methods Appl. Mech. Engrg. 193, 3767–3805. http://dx.doi.org/10.1016/j.cma.2004.02.009, URL https://www.sciencedirect.com/science/article/pii/S0045782504001422.

Aravas, N., Xenos, S., 2023. Implicit vs explicit gradient plasticity models: do they always remove mesh dependence in softening materials? Int. J. Solids Struct. 281, 112415. http://dx.doi.org/10.1016/j.ijsolstr.2023.112415, URL https://www.sciencedirect.com/science/article/pii/S0020768323003128.

Bai, Y., Wierzbicki, T., 2008. A new model of metal plasticity and fracture with pressure and lode dependence. Int. J. Plast. 24, 1071–1096. http://dx.doi.org/10.1016/j.ijplas.2007.09.004, URL https://www.sciencedirect.com/science/article/pii/S0749641907001246.

Barlo, A., Sigvant, M., Pérez, L., Islam, M., Pilthammar, J., 2022. A study of the boundary conditions in the iso-16630 hole expansion test. IOP Conf. Ser. Mater. Sci. Eng. 1238, 012031. http://dx.doi.org/10.1088/1757-899X/1238/1/012031.

Barsoum, I., Faleskog, J., 2007. Rupture mechanisms in combined tension and shear—Micromechanics. Int. J. Solids Struct. 44, 5481–5498. http://dx.doi.org/10.1016/j.ijsolstr.2007.01.010, URL https://www.sciencedirect.com/science/article/pii/S0020768307000182.

Bele, E., Goel, A., Pickering, E., Borstnar, G., Katsamenis, O., Pierron, F., Danas, K., Deshpande, V., 2017. Deformation mechanisms of idealised cermets under multi-axial loading. J. Mech. Phys. Solids 102, 80–100. http://dx.doi.org/10.1016/j.jmps.2017.01.002, URL https://www.sciencedirect.com/science/article/pii/S0022509616308146.

Benhizia, A., Kanit, T., Outtas, T., Madani, S., Imad, A., 2014. Computation of effective behavior of isotropic transverse composite in nonlinear problems. Mech. Res. Commun. 59, 6–13. http://dx.doi.org/10.1016/j.mechrescom.2014.03.005, URL https://www.sciencedirect.com/science/article/pii/S0093641314000305.

Bensaada, R., Kanit, T., Imad, A., Almansba, M., Saouab, A., 2022. Void-growth computational analysis in elastic–plastic porous materials. Int. J. Mech. Sci. 217, 107021. http://dx.doi.org/10.1016/j.ijmecsci.2021.107021, URL https://www.sciencedirect.com/science/article/pii/S0020740321007086.

Benzerga, A., Leblond, J.B., 2010. Ductile fracture by void growth to coalescence. Adv. Appl. Mech. 44, 169–305. http://dx.doi.org/10.1016/S0065-2156(10)44003-X, URL https://www.sciencedirect.com/science/article/pii/S006521561044003X.

Benzerga, A., Leblond, J.B., Needleman, A., Tvergaard, V., 2016. Ductile failure modeling. Int. J. Fract. 201, 29–80. http://dx.doi.org/10.1007/s10704-016-0142-6.

Bergo, S., Morin, D., Sture Hopperstad, O., 2021. Numerical implementation of a non-local gtn model for explicit fe simulation of ductile damage and fracture. Int. J. Solids Struct. 219–220, 134–150. http://dx.doi.org/10.1016/j.ijsolstr.2021.03.007, URL https://www.sciencedirect.com/science/article/pii/S0020768321000913.

Bilger, N., Auslender, F., Bornert, M., Moulinec, H., Zaoui, A., 2007. Bounds and estimates for the effective yield surface of porous media with a uniform or a nonuniform distribution of voids. Eur. J. Mech. A Solids 26, 810–836. http://dx.doi.org/10.1016/j.euromechsol.2007.01.004, URL https://www.sciencedirect.com/science/article/pii/S099775380700023X.

Bouby, C., Morin, L., Bignonnet, F., Dormieux, L., Kondo, D., 2023. On the thermodynamics consistency of Gurson's model and its computational implications. Int. J. Solids Struct. 279, 112359. http://dx.doi.org/10.1016/j.ijsolstr.2023.112359, URL https://www.sciencedirect.com/science/article/pii/S0020768323002561.

Cao, T.S., Mazière, M., Danas, K., Besson, J., 2015. A model for ductile damage prediction at low stress triaxialities incorporating void shape change and void rotation. Int. J. Solids Struct. 63, 240–263. http://dx.doi.org/10.1016/j.ijsolstr.2015.03.003, URL https://www.sciencedirect.com/science/article/pii/S0020768315001080.

Cheng, L., Danas, K., Constantinescu, A., Kondo, D., 2017. A homogenization model for porous ductile solids under cyclic loads comprising a matrix with isotropic and linear kinematic hardening. Int. J. Solids Struct. 121, 174–190. http://dx.doi.org/10.1016/j.ijsolstr.2017.05.024, URL https://www.sciencedirect.com/science/article/pii/S0020768317302354.

Chu, C., Needleman, A., 1980. Void nucleation effects in biaxially stretched sheets. J. Eng. Mater. Technol. 102, 249–256. http://dx.doi.org/10.1115/1.3224807.

Dæhli, L.E., Morin, D., Børvik, O.S., 2018. A lode-dependent Gurson model motivated by unit cell analyses. Eng. Fract. Mech. 190, 299–318. http://dx.doi.org/10.1016/j.engfracmech.2017.12.023, URL https://www.sciencedirect.com/science/article/pii/S0013794417306872.

Danas, K., 2008. Homogenization-Based Constitutive Models for Viscoplastic Porous Media with Evolving Microstructure (Ph.D. thesis). University of Pennsylvania.

Danas, K., Aravas, N., 2012. Numerical modeling of elasto-plastic porous materials with void shape effects at finite deformations. Composites B 43, 2544–2559. http://dx.doi.org/10.1016/j.compositesb.2011.12.011, URL https://www.sciencedirect.com/science/article/pii/S1359836812000029.

Danas, K., Idiart, M., Ponte Castañeda, P., 2008a. A homogenization-based constitutive model for two-dimensional viscoplastic porous media. C.R. Méch. 336, 79–90. http://dx.doi.org/10.1016/j.crme.2007.10.017, URL https://www.sciencedirect.com/science/article/pii/S1631072107001994.

Danas, K., Idiart, M., Ponte Castañeda, P., 2008b. A homogenization-based constitutive model for isotropic viscoplastic porous media. Int. J. Solids Struct. 45, 3392–3409. http://dx.doi.org/10.1016/j.ijsolstr.2008.02.007, URL https://www.sciencedirect.com/science/article/pii/S0020768308000656.

Danas, K., Ponte Castañeda, P., 2009a. A finite-strain model for anisotropic viscoplastic porous media: I – theory. Eur. J. Mech. A Solids 28, 387–401. http://dx.doi.org/10.1016/j.euromechsol.2008.11.002, URL https://www.sciencedirect.com/science/article/pii/S0997753808001150.

Danas, K., Ponte Castañeda, P., 2009b. A finite-strain model for anisotropic viscoplastic porous media: II – applications. Eur. J. Mech. A Solids 28, 402–416. http://dx.doi.org/10.1016/j.euromechsol.2008.11.003, URL https://www.sciencedirect.com/science/article/pii/S0997753808001149.

Danas, K., Ponte Castañeda, P., 2012. Influence of the Lode parameter and the stress triaxiality on the failure of elasto-plastic porous materials. Int. J. Solids Struct. 49, 1325–1342. http://dx.doi.org/10.1016/j.ijsolstr.2012.02.006, URL https://www.sciencedirect.com/science/article/pii/S0020768312000467.

Dunand, M., Mohr, D., 2014. Effect of Lode parameter on plastic flow localization after proportional loading at low stress triaxialities. J. Mech. Phys. Solids 66, 133–153. http://dx.doi.org/10.1016/j.jmps.2014.01.008, URL https://www.sciencedirect.com/science/article/pii/S0022509614000180.

El Moumen, A., Imad, A., Kanit, T., Hilali, E., El Minor, H., 2014. A multiscale approach and microstructure design of the elastic composite behavior reinforced with natural particles. Composites B 66, 247–254. http://dx.doi.org/10.1016/j.compositesb.2014.05.008, URL https://www.sciencedirect.com/science/article/pii/S1359836814002066.

El Moumen, A., Kanit, T., Imad, A., El Minor, H., 2015a. Computational thermal conductivity in porous materials using homogenization techniques: Numerical and statistical approaches. Comput. Mater. Sci. 97, 148–158. http://dx.doi.org/10.1016/j.commatsci.2014.09.043, URL https://www.sciencedirect.com/science/article/pii/S0927025614006685.

El Moumen, T., Imad, A., El Minor, H., 2015b. Effect of reinforcement shape on physical properties and representative volume element of particles-reinforced composites: Statistical and numerical approaches. Mech. Mater. 83, 1–16. http://dx.doi.org/10.1016/j.mechmat.2014.12.008, URL https://www.sciencedirect.com/science/article/pii/S016766361400221X.

Eshelby, J.D., 1957. The determination of the elastic field of an ellipsoidal inclusion, and related problems. Proc. R. Soc. Lond. Ser. A Math. Phys. Eng. Sci. 241, 376–396, URL http://www.jstor.org/stable/100095.

Gatt, J.M., Monerie, Y., Laux, D., Baron, D., 2005. Elastic behavior of porous ceramics: application to nuclear fuel materials. J. Nucl. Mater. 336, 145–155. http://dx.doi.org/10.1016/j.jnucmat.2004.09.009, URL https://www.sciencedirect.com/science/article/pii/S0022311504006920.

Gologanu, M., Leblond, J.B., Devaux, J., 1993. Approximate models for ductile metals containing non-spherical voids-case of axisymmetric prolate ellipsoidal cavities. J. Mech. Phys. Solids 41, 1723–1754. http://dx.doi.org/10.1016/0022-5096(93)90029-F, URL https://www.sciencedirect.com/science/article/pii/002250969390029F.

Gologanu, M., Leblond, J.B., Devaux, J., 1994. Approximate models for ductile metals containing non-spherical voids-case of axisymmetric oblate ellipsoidal cavities. J. Eng. Mater. Technol. 116, 290–297. http://dx.doi.org/10.1115/1.2904290.

Gologanu, M., Leblond, J.B., Perrin, G., Devaux, J., 1997. Recent Extensions of Gurson's Model for Porous Ductile Metals. Springer Vienna, Vienna, pp. 61–130. http://dx.doi.org/10.1007/978-3-7091-2662-2_2.

Gurson, A.L., 1977. Continuum theory of ductile rupture by void nucleation and growth: Part I—yield criteria and flow rules for porous ductile media. J. Eng. Mater. Technol. 99, 2–15. http://dx.doi.org/10.1115/1.3443401.

Hashin, Z., Shtrikman, S., 1963. A variational approach to the theory of the elastic behaviour of multiphase materials. J. Mech. Phys. Solids 11, 127–140. http://dx.doi.org/10.1016/0022-5096(63)90060-7, URL https://www.sciencedirect.com/science/article/pii/0022509663900607.

He, Z., Zhu, H., Hu, Y., 2021. An improved shear modified GTN model for ductile fracture of aluminium alloys under different stress states and its parameters identification. Int. J. Mech. Sci. 192, 106081. http://dx.doi.org/10.1016/j.ijmecsci.2020.106081, URL https://www.sciencedirect.com/science/article/pii/S0020740320323055.

Hill, R., 1963. Elastic properties of reinforced solids: Some theoretical principles. J. Mech. Phys. Solids 11, 357–372.

Holte, I., Nielsen, K., Martínez-Pañeda, C., 2023. A micro-mechanics based extension of the gtn continuum model accounting for random void distributions. Eur. J. Mech. A Solids 105123. http://dx.doi.org/10.1016/j.euromechsol.2023.105123, URL https://www.sciencedirect.com/science/article/pii/S0997753823002152.

Hooshmand-Ahoor, Z., Tarantino, M., Danas, K., 2022. Mechanically-grown morphogenesis of Voronoi-type materials: Computer design, 3D-printing and experiments. Mech. Mater. 173, 104432. http://dx.doi.org/10.1016/j.mechmat.2022.104432, URL https://www.sciencedirect.com/science/article/pii/S0167663622002010.

Idiart, M., Ponte Castañeda, P., 2007. Variational linear comparison bounds for nonlinear composites with anisotropic phases, I. General results. Proc. Math. Phys. Eng. Sci. 463, 907–924, URL http://www.jstor.org/stable/20209159.

ISO 16630:2017, 2017. Metallic Materials — Sheet and Strip — Hole Expanding Test, ISO 16630:2017 ed. International Organization for Standardization, URL https://www.iso.org/standard/69771.html.

Kailasam, M., Ponte Castañeda, P., Willis, J.R., 1997. The effect of particle size, shape, distribution and their evolution on the constitutive response of nonlinearly viscous composites. Phil. Trans. R. Soc. B 355, 1835–1852. http://dx.doi.org/10.1098/rsta.1997.0092, URL https://royalsocietypublishing.org/doi/abs/10.1098/rsta.1997.0092.

Kailasam, M., Ponte Castañeda, P., 1998. A general constitutive theory for linear and nonlinear particulate media with microstructure evolution. J. Mech. Phys. Solids 46, 427–465. http://dx.doi.org/10.1016/S0022-5096(97)00095-1, URL https://www.sciencedirect.com/science/article/pii/S0022509697000951.

Kanit, T., Forest, S., Galliet, I., Mounoury, V., Jeulin, D., 2003. Determination of the size of the representative volume element for random composites: statistical and numerical approach. Int. J. Solids Struct. 40, 3647–3679. http://dx.doi.org/10.1016/S0020-7683(03)00143-4, URL https://www.sciencedirect.com/science/article/pii/S0020768303001434.

Khan, I., Benzerga, A., Needleman, A., 2023. A shear modified enhanced gurson constitutive relation and implications for localization. J. Mech. Phys. Solids 171, 105153. http://dx.doi.org/10.1016/j.jmps.2022.105153, URL https://www.sciencedirect.com/science/article/pii/S0022509622003295.

Leblond, J.B., Perrin, G., Suquet, P., 1994. Exact results and approximate models for porous viscoplastic solids. Int. J. Plast. 10, 213–235. http://dx.doi.org/10.1016/0749-6419(94)90001-9, URL https://www.sciencedirect.com/science/article/pii/0749641994900019.

Limodin, N., Dahdah, N., Wang, L., El Bartali, J.F., Buffiere, J.Y., Charkaluk, E., 2023. Characterisation of 3D strain heterogeneity at the microstructure scale during low cycle fatigue of an AlSi7Cu3Mg alloy at 250 °C. Int. J. Fatigue 172, 107476. http://dx.doi.org/10.1016/j.ijfatigue.2022.107476, URL https://www.sciencedirect.com/science/article/pii/S0142112322007265.

Lopez-Pamies, O., Goudarzi, T., Danas, K., 2013. The nonlinear elastic response of suspensions of rigid inclusions in rubber: II—A simple explicit approximation for finite-concentration suspensions. J. Mech. Phys. Solids 61, 19–37. http://dx.doi.org/10.1016/j.jmps.2012.08.013.

Luo, H., Hooshmand-Ahoor, Z., Danas, K., Diani, J., 2023. Numerical estimation via remeshing and analytical modeling of nonlinear elastic composites comprising a large volume fraction of randomly distributed spherical particles or voids. Eur. J. Mech. A Solids 105076. http://dx.doi.org/10.1016/j.euromechsol.2023.105076, URL https://www.sciencedirect.com/science/article/pii/S0997753823001687.

Madou, K., Leblond, J.B., 2012a. A Gurson-type criterion for porous ductile solids containing arbitrary ellipsoidal voids—I: Limit-analysis of some representative cell. J. Mech. Phys. Solids 60, 1020–1036. http://dx.doi.org/10.1016/j.jmps.2011.11.008, URL https://www.sciencedirect.com/science/article/pii/S0022509611002201.

Madou, K., Leblond, J.B., 2012b. A Gurson-type criterion for porous ductile solids containing arbitrary ellipsoidal voids—II: Determination of yield criterion parameters. J. Mech. Phys. Solids 60, 1037–1058. http://dx.doi.org/10.1016/j.jmps.2012.01.010, URL https://www.sciencedirect.com/science/article/pii/S002250961200018X.

Madou, K., Leblond, J.B., Morin, L., 2013. Numerical studies of porous ductile materials containing arbitrary ellipsoidal voids – II: Evolution of the length and orientation of the void axes. Eur. J. Mech. A Solids 42, 490–507. http://dx.doi.org/10.1016/j.euromechsol.2013.06.005, URL https://www.sciencedirect.com/science/article/pii/S0997753813000703.

Mbiakop, A., Constantinescu, A., Danas, K., 2015a. A model for porous single crystals with cylindrical voids of elliptical cross-section. Int. J. Solids Struct. 64-65, 100–119. http://dx.doi.org/10.1016/j.ijsolstr.2015.03.017, URL https://www.sciencedirect.com/science/article/pii/S0020768315001328.

Mbiakop, A., Constantinescu, A., Danas, K., 2015b. An analytical model for porous single crystals with ellipsoidal voids. J. Mech. Phys. Solids 84, 436–467. http://dx.doi.org/10.1016/j.jmps.2015.07.011.

Meyer, C., 2000. Matrix Analysis and Applied Linear Algebra. Society for Industrial and Applied Mathematics, https://books.google.gr/books?id=m7W2748ynMcC.

Meynard, J., Ibrahim, M., Monnier, A., Bornert, M., Castelier, E., Duguay, C., Gărăjeu, R., 2022. Effective properties of an isotropic solid weakened by micro-cracks located at inter-granular boundaries. J. Mech. Phys. Solids 158, 104647. http://dx.doi.org/10.1016/j.jmps.2021.104647, URL https://www.sciencedirect.com/science/article/pii/S0022509621002866.

Michel, J., Moulinec, H., Suquet, P., 1999. Effective properties of composite materials with periodic microstructure: a computational approach. Comput. Methods Appl. Mech. Engrg. 172, 109–143. http://dx.doi.org/10.1016/S0045-7825(98)00227-8, URL https://www.sciencedirect.com/science/article/pii/S0045782598002278.

Michel, J.C., Suquet, P., 1992. The constitutive law of nonlinear viscous and porous materials. J. Mech. Phys. Solids 40, 783–812. http://dx.doi.org/10.1016/0022-5096(92)90004-L, URL https://www.sciencedirect.com/science/article/pii/002250969290004L.

Moakher, M., Norris, A., 2006. The closest elastic tensor of arbitrary symmetry to an elasticity tensor of lower symmetry. J. Elasticity 85, 215–263. http://dx.doi.org/10.1007/s10659-006-9082-0.

Monchiet, V., 2006. Contributions à la modélisation micromécanique de l'endommagement et de la fatigue des métaux ductiles (Ph.D. thesis). University of Lille I, URL http://www.theses.fr/2006LIL10129.

Morin, L., Leblond, J.B., Mohr, D., Kondo, D., 2017. Prediction of shear-dominated ductile fracture in a butterfly specimen using a model of plastic porous solids including void shape effects. Eur. J. Mech. A Solids 61, 433–442. http://dx.doi.org/10.1016/j.euromechsol.2016.10.014, URL https://www.sciencedirect.com/science/article/pii/S0997753816301176.

Morin, L., Leblond, J.B., Tvergaard, V., 2016. Application of a model of plastic porous materials including void shape effects to the prediction of ductile failure under shear-dominated loadings. J. Mech. Phys. Solids 94, 148–166. http://dx.doi.org/10.1016/j.jmps.2016.04.032, URL https://www.sciencedirect.com/science/article/pii/S0022509616302393.

Mura, T., 1987. Micromechanics of Defects in Solids, Second, revised ed. Kluwer, Dordrecht.

Nahshon, K., Hutchinson, J.W., 2008. Modification of the Gurson model for shear failure. Eur. J. Mech. A Solids 27, 1–17. http://dx.doi.org/10.1016/j.euromechsol.2007.08.002, URL https://www.sciencedirect.com/science/article/pii/S0997753807000721.

Nielsen, K., Dahl, J., Tvergaard, V., 2012. Collapse and coalescence of spherical voids subject to intense shearing: Studied in full 3D. Int. J. Fract. 177, 97–108. http://dx.doi.org/10.1007/s10704-012-9757-4.

Nielsen, K.L., Tvergaard, V., 2011. Failure by void coalescence in metallic materials containing primary and secondary voids subject to intense shearing. Int. J. Solids Struct. 48, 1255–1267. http://dx.doi.org/10.1016/j.ijsolstr.2011.01.008, URL https://www.sciencedirect.com/science/article/pii/S0020768311000175.

Noell, P.J., Carroll, J.D., Boyce, B.L., 2018. The mechanisms of ductile rupture. Acta Mater. 161, 83–98. http://dx.doi.org/10.1016/j.actamat.2018.09.006, URL https://www.sciencedirect.com/science/article/pii/S1359645418307006.

Papadioti, I., Danas, K., Aravas, N., 2016. A methodology for the estimation of the effective yield function of isotropic composites. Int. J. Solids Struct. 87, 120–138. http://dx.doi.org/10.1016/j.ijsolstr.2016.02.022, URL https://www.sciencedirect.com/science/article/pii/S0020768316000846.

Pardoen, T., Hutchinson, J., 2000. An extended model for void growth and coalescence. J. Mech. Phys. Solids 48, 2467–2512. http://dx.doi.org/10.1016/S0022-5096(00)00019-3, URL https://www.sciencedirect.com/science/article/pii/S0022509600000193.

Ponte Castañeda, P., 1991. The effective mechanical properties of nonlinear isotropic composites. J. Mech. Phys. Solids 39, 45–71. http://dx.doi.org/10.1016/0022-5096(91)90030-R, URL https://www.sciencedirect.com/science/article/pii/002250969190030R.

Ponte Castañeda, P., 2012. Bounds for nonlinear composites via iterated homogenization. J. Mech. Phys. Solids 60, 1583–1604. http://dx.doi.org/10.1016/j.jmps.2012.05.004, URL https://www.sciencedirect.com/science/article/pii/S0022509612001093.

Rousselier, G., 2022. Lode-dependent second porosity in porous plasticity for shear-dominated loadings. Int. J. Plast. 159, 103446. http://dx.doi.org/10.1016/j.ijplas.2022.103446, URL https://www.sciencedirect.com/science/article/pii/S0749641922002248.

Shen, W., Lin, J., Zhu, Q., Monchiet, V., Kondo, D., 2011. Macroscopic yield criterion for ductile materials containing randomly oriented spheroidal cavities. Int. J. Damage Mech. 20, 1198–1216. http://dx.doi.org/10.1177/1056789510395552.

Song, D., Ponte Castañeda, P., 2018. A multi-scale homogenization model for fine-grained porous viscoplastic polycrystals: I – finite-strain theory. J. Mech. Phys. Solids 115, 102–122. http://dx.doi.org/10.1016/j.jmps.2018.03.001, URL https://www.sciencedirect.com/science/article/pii/S0022509618300322.

Srivastava, A., Ponson, L., Osovski, S., Bouchaud, E., Tvergaard, V., Needleman, A., 2014. Effect of inclusion density on ductile fracture toughness and roughness. J. Mech. Phys. Solids 63, 62–79. http://dx.doi.org/10.1016/j.jmps.2013.10.003, URL https://www.sciencedirect.com/science/article/pii/S0022509613002111.

Suquet, P.M., 1987. Elements of homogenization for inelastic solid mechanics. In: Sanchez-Palencia, E., Zaoui, A. (Eds.), Homogenization Techniques for Composite Media. Springer Berlin Heidelberg, Berlin, Heidelberg, pp. 193–198. http://dx.doi.org/10.1007/3-540-17616-0_15.

Tarantino, M., Zerhouni, O., Danas, K., 2019. Random 3D-printed isotropic composites with high volume fraction of pore-like polydisperse inclusions and near-optimal elastic stiffness. Acta Mater. 175, 331–340. http://dx.doi.org/10.1016/j.actamat.2019.06.020.

Tuhami, A.E.O., Feld-Payet, S., Quilici, S., Osipov, N., Besson, J., 2022. A two characteristic length nonlocal gtn model: Application to cup–cone and slant fracture. Mech. Mater. 171, 104350. http://dx.doi.org/10.1016/j.mechmat.2022.104350, URL https://www.sciencedirect.com/science/article/pii/S0167663622001272.

Tvergaard, V., 1981. Influence of voids on shear band instabilities under plane strain conditions. Int. J. Fract. 17, 389–407, URL https://api.semanticscholar.org/CorpusID:136549697.

Tvergaard, V., 2009. Behaviour of voids in a shear field. Int. J. Fract. 158, 41–49. http://dx.doi.org/10.1007/s10704-009-9364-1.

Tvergaard, V., Needleman, A., 1984. Analysis of the cup-cone fracture in a round tensile bar. Acta Metall. 32, 157–169. http://dx.doi.org/10.1016/0001-6160(84)90213-X, URL https://www.sciencedirect.com/science/article/pii/000161608490213X.

Vincent, P.G., Monerie, Y., 2008. Yield criterion for a rigid-ideally plastic material with randomly oriented cracks. C.R. Mech. 336, 297–303. http://dx.doi.org/10.1016/j.crme.2007.11.020.

Wang, S., Faleskog, J., 2023. A non-local gtn model with two length scales – application to ductile failure in a wide range of stress triaxiality. Eur. J. Mech. A Solids 105056. http://dx.doi.org/10.1016/j.euromechsol.2023.105056, URL https://www.sciencedirect.com/science/article/pii/S0997753823001481.

Wang, L., Limodin, N., El Bartali, A., Charkaluk, E., 2021. Coupling of X-ray computed tomography and surface in situ analysis combined with digital image correlation method to study low cycle fatigue damage micromechanisms in lost foam casting A319 alloy. Fatigue Fract. Eng. Mater. Struct. 44, 916–932. http://dx.doi.org/10.1111/ffe.13402, URL https://onlinelibrary.wiley.com/doi/abs/10.1111/ffe.13402, arXiv:https://onlinelibrary.wiley.com/doi/pdf/10.1111/ffe.13402.

Weyl, H., 1946. The Classical Groups: Their Invariants and Representations. Vol. 1. Princeton University Press.

Willis, J.R., 1977. Bounds and self-consistent estimates for the overall properties of anisotropic composites. J. Mech. Phys. Solids 25, 185–202. http://dx.doi.org/10.1016/0022-5096(77)90022-9, URL https://www.sciencedirect.com/science/article/pii/0022509677900229.

Willis, J.R., 1980. A polarization approach to the scattering of elastic waves – II. Multiple scattering from inclusions. J. Mech. Phys. Solids 28, 307–327. http://dx.doi.org/10.1016/0022-5096(80)90022-8, URL https://www.sciencedirect.com/science/article/pii/0022509680900228.

Willis, J.R., 1981. Variational and related methods for the overall properties of composites. Adv. Appl. Mech. 21, 1–78. http://dx.doi.org/10.1016/S0065-2156(08)70330-2, URL https://www.sciencedirect.com/science/article/pii/S0065215608703302.

Willis, J.R., 1982. Elasticity theory of composites. Mechanics of Solids. Pergamon, Oxford, pp. 653–686. http://dx.doi.org/10.1016/B978-0-08-025443-2.50025-2, URL https://www.sciencedirect.com/science/article/pii/B9780080254432500252,

Willis, J.R., 1991. On methods for bounding the overall properties of nonlinear composites. J. Mech. Phys. Solids 39, 73–86. http://dx.doi.org/10.1016/0022-5096(91)90031-I, URL https://www.sciencedirect.com/science/article/pii/002250969190031I.

Zerhouni, O., Brisard, S., Danas, K., 2021. Quantifying the effect of two-point correlations on the effective elasticity of specific classes of random porous materials with and without connectivity. Internat. J. Engrg. Sci. 166, 103520. http://dx.doi.org/10.1016/j.ijengsci.2021.103520, URL https://www.sciencedirect.com/science/article/pii/S0020722521000677.

Zerhouni, O., Tarantino, M., Danas, K., 2019. Numerically-aided 3D printed random isotropic porous materials approaching the Hashin–Shtrikman bounds. Composites B 156, 344–354. http://dx.doi.org/10.1016/j.compositesb.2018.08.032, URL https://www.sciencedirect.com/science/article/pii/S1359836818310710.

Zhou, J., Gao, X., Sobotka, J.C., Webler, B.A., Cockeram, B.V., 2014. On the extension of the Gurson-type porous plasticity models for prediction of ductile fracture under shear-dominated conditions. Int. J. Solids Struct. 51, 3273–3291. http://dx.doi.org/10.1016/j.ijsolstr.2014.05.028, URL https://www.sciencedirect.com/science/article/pii/S0020768314002224.